A Multi-Fidelity Boundary Element Method for Structural Reliability Analysis with Higher-Order Sensitivities

Llewellyn Morse*, Zahra Sharif Khodaei, M.H. Aliabadi

Department of Aeronautics, Imperial College London, South Kensington Campus, City and Guilds Building, Exhibition Road, SW7 2AZ, London, UK

Abstract

A novel multi-fidelity modelling methodology for structural reliability analysis using the Boundary Element Method (BEM) with an Implicit Differentiation Method (IDM) is presented. Reliability analyses are conducted with methods such as Monte Carlo Simulation (MCS) and the First-Order Reliability Method (FORM). The higher-order sensitivities of the elastostatic Boundary Element Method equations with respect to changes in several geometric variables have been derived for the first time for use with the IDM for the purpose of conducting reliability analyses with the Second-Order Reliability Method (SORM), a more accurate alternative to FORM for problems with non-linear limit state functions. Multi-fidelity formulations involving the IDM have also been derived for the first time, making use of the metamodelling technique *Kriging*. The use of multi-fidelity modelling enables the creation of a model that has similar accuracy to a high-fidelity model, but with a computational cost similar to that of a low-fidelity model. By combining the accuracy of the IDM with the efficiency of multi-fidelity modelling the proposed methodology has the capability to be very effective when used for structural reliability analysis. The IDM is validated through a numerical example for which the analytical solution is known. A further two numerical examples featuring an I-beam section and a triangular support bracket with a large number of variables are also investigated. Results show that the employed multi-fidelity models were up to 6000 times faster in terms of CPU-time than the high-fidelity model, while also providing probabilities of failure that were up to 2225 times more accurate than the low-fidelity model. Overall, it has been shown that the use of the proposed IDM/multi-fidelity modelling methodology significantly improved the efficiency and accuracy of the above reliability analysis techniques when applied to complex problems involving a large number of random variables under high levels of uncertainty.

Keywords: Structural reliability analysis; Multi-fidelity modelling; Kriging; Sensitivity Analysis; Boundary Element Method (BEM); Implicit Differentiation Method (IDM)

---

1. Introduction

Reliability analysis offers engineers many advantages when designing structures. It enables engineers to understand how uncertainties in various design parameters influence the reliability of their structure, and allows them to focus on the most critical areas of their design and helps them identify ways of improving its overall

---

*Corresponding author

Email addresses: llewellyn.morse12@imperial.ac.uk (L. Morse), z.sharif-khodaei@imperial.ac.uk (Z. Sharif Khodaei), m.h.aliabadi@imperial.ac.uk (M.H. Aliabadi)

Abbreviations: Boundary Element Method (BEM); Finite Element Method (FEM); Finite Difference Method (FDM); Implicit Differentiation Method (IDM); First Order Reliability Method (FORM); Second Order Reliability Method (SORM); Monte Carlo Simulation (MCS); Low Fidelity Model (LFM); High-fidelity Model (HFM); Multi-Fidelity Model (MFM)

Preprint submitted to Elsevier *March 25, 2019*

reliability. Among the methods used for structural reliability analysis are statistical methods and non-statistical methods [1]. Statistical methods include techniques such as Monte Carlo Simulation (MCS) which simulates the limit state function directly, while non-statistical methods include techniques such as the First-Order Reliability Method (FORM) and the Second-Order Reliability Method (SORM), which approximate the limit state function using first-order and second-order Taylor series expansions respectively. For many problems, particularly complex ones involving highly non-linear limit state functions, SORM is often more accurate than FORM due its use of higher-order sensitivities, allowing for a better approximatation of reliability in these cases. More details of these methods can be found in many books on the topic of reliability analysis [2, 3, 4].

The Boundary Element Method (BEM) has shown itself to be an effective tool for the analysis of engineering structures. Regarding its application to the topic of structural reliability analysis, it has several features that make it a useful alternative to the Finite Element Method (FEM). Such features include the reduction of the dimensionality of the problem and its ability to obtain a similar level of accuracy to the FEM while using a much coarser mesh. Re-meshing can also be significantly easier with the BEM due to its inherent boundary-only discretization, allowing for sensitivity analyses involving geometric variables to be more efficiently carried out. These advantages, and others, are discussed in more detail in previous works concerning sensitivity analyses with geometric variables involving: elastostatic structures [1, 5, 6], fatigue crack growth [7, 8, 9], creep [10], plate bending [11], and topology optimization [12].

Two approaches that have been used with the BEM to obtain the sensitivities required by FORM and SORM are the Finite Difference Method (FDM) [6, 7] and another which involves the use of an Implicit Differentiation Method (IDM) [5, 13, 14]. The FDM involves the use of finite differences to obtain derivatives. Being a relatively crude method, its accuracy is heavily dependent on the stepsize used [15]. In many cases, the optimal stepsize can only be determined through a trial-and-error approach, making the FDM computationally expensive to carry out. The use of an IDM, on the other hand, involves the direct differentiation of the discretised BEM equations, resulting in a solution without the need of a trial-and-error approach, significantly improving the efficiency of the formulations. This direct differentiation is highly efficient as only those parts of the BEM equations which are influenced by a change in a variable need to be re-evaluated. The result is a significant improvement in efficiency, as only some equations will need to be updated during the reliability analyses. A comprehensive overview of the application of the BEM to structural analysis, as well as an introduction to the IDM used in this work, can be found in [16].

In the context of this work, surrogate modelling or metamodelling, refers to the process of substituting a real model for a 'surrogate' model. The surrogate model is typically created by evaluating the response of the real model at several points, called design points/sites. Types of metamodels that have been employed in the past with regards to structural reliability analysis include polynomials [6, 10, 17, 18, 19], Kriging [20, 21, 22], and Neural Networks (NNs) [23, 24]. Although surrogate models are not as accurate as the real model over the entire domain being investigated, they can act as very effective substitutes for the real model over a small part of the domain. This makes them very useful for reliability analyses.

Multi-fidelity modelling is a specific type of metamodelling, whereby a surrogate model approximating a high-fidelity model (HFM) is created by evaluating both the response of the HFM and a low-fidelity model (LFM) at several design sites, within the domain being investigated. In the context of numerical computational methods such as the FEM and the BEM, LFMs and HFMs refer to models with coarse and fine element discretisations respectively. The aim of multi-fidelity modelling is to provide a multi-fidelity model (MFM) that is of similar accuracy to the HFM over the required domain, but at a computational cost similar to that of the LFM. Two recent reviews of metamodelling techniques have been undertaken by Simpson *et al* [25] and Bhosekar *et al* [26] . Multi-fidelity models created in the past include those based on polynomials [27, 28, 6], and those based on Kriging [29, 30, 20]. Due to its many advantages, multi-fidelity modelling has found extensive use with the FEM, with notable examples being [27, 28, 20]. However, its application to structural reliability analysis has received limited attention, with one known example being [20] for the XFEM (Extended Finite Element Method). Examples of the application of multi-fidelity modelling with the BEM are limited, one known example is [6].

Two types of surrogate models that have been used in the past for multi-fidelity modelling with structural reliability analysis are Kriging [20] and response surfaces [6]. Lefebvre *et al* [20] employed a sophisticated approach to multi-fidelity modelling based structural reliability analysis through the use of co-Kriging, a variant of Kriging that takes into account data of different fidelities. The work conducted in [6] built on the work presented by Vitali *et al* [27] with the FEM and applied multi-fidelity modelling to structural reliability analysis using the BEM. MFMs in the form of response surfaces were created using the response of a HFM and a LFM at a number of design points. Direct MFMs which involved directly calling the LFM, and indirect models which involved approximating the LFM as a response surface, were created. It was found that the direct MFMs provided the greatest improvement in accuracy over the LFM when used with FORM, SORM, and MCS.

The main objective of this work concerns the development of a multi-fidelity modelling methodology with the boundary element method for structural reliability analysis. This involves the derivation of multi-fidelity modelling formulations for the IDM, via Kriging. Due to the significant benefits that multi-fidelity modelling can provide, as well as the inherent advantages of the BEM, particularly for structural reliability analysis, the development of multi-fidelity modelling formulations for the BEM is an area of great interest. The employed IDM, involving the direct differentiation of the BEM equations, represents a significant improvement in efficiency over the FDM used in the past. It is used in this work as an alternative to the FDM for the evaluation of the sensitivities necessary for FORM. The necessary formulations for the IDM with SORM have also been derived. Multi-fidelity modelling is achieved through the use of Kriging, which involves interpolating between design points. It is therefore more suitable than other modelling techniques for the creation of multi-fidelity models with numerical methods such as the BEM. The use of Kriging allows for accurate multi-fidelity models to be created, improving the efficiency of the reliability analysis formulations. In summary, the specific main novel contributions of this current work are:

- The higher-order sensitivities of a structure to changes in certain design variables are derived for the first time with the IDM for the BEM. These higher-order sensitivities are required by the Second-Order Reliability Method (SORM), an advanced method for structural reliability analysis. Since SORM involves the calculation of the second-order derivatives of the response of a structure, it can more accurately approximate non-linear limit state functions, such as those in this work. Previous applications with an IDM for the BEM have been limited to the First Order Reliability Method (FORM).

- Multi-fidelity modelling formulations for an IDM with the BEM have been derived for the first time. The significant improvement in efficiency that could be gained from the use of multi-fidelity modelling, added to the accuracy of the IDM, has the potential to make the proposed multi-fidelity/IDM methodology very effective when applied to structural reliability analysis.

2. Reliability analysis formulations

The criteria for determining structural failure used in this work is based on the maximum stress present in a BEM model. The location of maximum stress in the structure is termed point A. If the maximum stress in the structure, σ_A, exceeds the material strength, σ_c, then the structure is assumed to have failed. The boundary between the structure failing and not-failing is defined as a limit state. This can be represented mathematically as a limit state function (LSF) or performance function [3], $g(\mathbf{Z})$:

$$g(\mathbf{Z}) = \sigma_c - \sigma_A(\mathbf{X}) \tag{1}$$

where $\mathbf{Z}$ is a size q vector containing all of the design/random variables under investigation, and $\mathbf{X}$ ($\mathbf{X} \subseteq \mathbf{Z}$) is a size n ($n = q - 1$) vector of the design variables that influence σ_A. In this work, $\mathbf{X}$ is identical to $\mathbf{Z}$ but excludes σ_c since it does not influence σ_A. All other variables in $\mathbf{X}$ are assumed to influence σ_A.

The reliability, P_R, of a structure can be determined by evaluating the following integral:

$$P_R = 1 - P_F = P\{g(\mathbf{Z}) > 0\} = \int\limits_{g(\mathbf{Z})>0} f_{\mathbf{Z}}(\mathbf{Z}) d\mathbf{Z} \tag{2}$$

where $f_{\mathbf{Z}}(\mathbf{Z})$ is the joint PDF of $\mathbf{Z}$. P_F and P_R involve integrating $f_{\mathbf{Z}}(\mathbf{Z})$ over the regions defined by $g(\mathbf{Z}) < 0$ (the failure region) and $g(\mathbf{Z}) > 0$ (the safe region) respectively. All of the random variables are assumed to be mutually independent. The direct evaluation of the above integral is usually very difficult since it can be multidimensional if many random variables are involved. The integration boundary $g(\mathbf{Z}) = 0$ can also be multidimensional and is usually a non-linear function.

There are several methods that can be used to evaluate this integral; MCS, which involves sampling from the distribution of each random variable , and FORM and SORM, which attempt to simplify the integration.

2.1. Monte Carlo Simulation (MCS)

MCS involves randomly sampling from known probability distributions to determine an unknown probability distribution [2]. If $\mathbf{Z} = (\mathrm{Z}_1, \mathrm{Z}_2, \ldots, \mathrm{Z}_q)$ is a vector of known random variables, and if $y = h(\mathbf{Z})$, where y is a random variable with an unknown probability distribution and h is some process or function, then the variables in $\mathbf{Z}$ can be randomly sampled per their probability distributions and used as the inputs to h and a value for y can be obtained. This is repeated many times until a histogram can be created of y, allowing us to estimate its probability distribution.

For each simulation, the variables in $\mathbf{Z}$ are randomly sampled from their probability distributions, with the samples of the variables in $\mathbf{X}$ being used as inputs to a BEM model to evaluate σ_A. If $g(\mathbf{Z}) < 0$ ($\sigma_A(\mathbf{X}) > \sigma_c$) for a simulation, then the structure is assumed to have failed for that simulation. After a certain number of simulations have been carried out, N_{MCS}, the total number of simulations in which the structure failed, N_F, can be determined and the failure probability, P_F, can be calculated as:

$$P_F = \frac{N_F}{N_{MCS}} \tag{3}$$

Reliability can be calculated as:

$$P_R = 1 - P_F \tag{4}$$

Because MCS is a simple brute-force sampling method, it can be used as a benchmark to validate the results obtained from the LSF approximation methods, FORM and SORM.

2.2. First Order Reliability Method (FORM)

The first order reliability method (FORM) used in this work refers to the advanced first-order second-moment (AFOSM) method for non-linear limit state functions. There are two steps that FORM takes to make the integration in equation (2) more manageable. The first step involves simplifying $f_{\mathbf{Z}}(\mathbf{Z})$ such that its contours are more regular and symmetric. This is achieved by transforming the random variables $\mathbf{Z} = (\mathrm{Z}_1, \mathrm{Z}_2, \dots, \mathrm{Z}_q)$ from $\mathbf{Z}$-space into $\mathbf{U}$-space, the standard normal space. Equation (1) can then be represented in terms of $\mathbf{U}$ as $g(\mathbf{U})$. Equation (2) can now be written as:

$$P_R = 1 - P_F = P\{g(\mathbf{U}) > 0\} = \int\limits_{g(\mathbf{U})>0} f_{\mathbf{U}}(\mathbf{U}) d\mathbf{U} \tag{5}$$

where $f_{\mathbf{U}}(\mathbf{U})$ is the joint PDF of $\mathbf{U}$. As a result of this transformation to $\mathbf{U}$-space, the contours of the integrand $f_{\mathbf{U}}(\mathbf{U})$ are now concentric circles about the origin (for two random variables) or hyperspheres (for a higher number of random variables) [2].

The second step involves approximating the integration boundary $g(\mathbf{U}) = 0$ as a first-order Taylor expansion:

$$g(\mathbf{U}) \approx g(\mathbf{U}^*) + \nabla g(\mathbf{U}^*)(\mathbf{U} - \mathbf{U}^*)^T \tag{6}$$

where $\mathbf{U}^* = (\mathrm{U}_1^*, \mathrm{U}_2^*, \dots \mathrm{U}_q^*)$ is the expansion point. $\nabla g(\mathbf{U}^*)$ is:

$$\nabla g(\mathbf{U}^*) = \left(\frac{\partial g(\mathbf{U})}{\partial \mathrm{U}_1}, \frac{\partial g(\mathbf{U})}{\partial \mathrm{U}_2}, \dots, \frac{\partial g(\mathbf{U})}{\partial \mathrm{U}_q} \right) \Bigg|_{\mathbf{U}^*} \tag{7}$$

To minimize the accuracy lost by this approximation it is necessary to expand g($\mathbf{U}$) at the point $\mathbf{U}^*$ that contributes the most to the integration seen in equation (5) and so will be the point that corresponds to the highest probability density. This point is termed the most probable point (MPP) [2] and is the point along the integration boundary $g(\mathbf{U}) = 0$ that is closest to the origin of $\mathbf{U}$-space. The distance between the MPP and the origin of $\mathbf{U}$-space is termed the reliability index β. β is related to the probability of failure P_F and reliability P_R in the following manner:

$$P_R = 1 - P_F = 1 - \Phi(-\beta) = \Phi(\beta) \tag{8}$$

where Φ denotes the standard normal cumulative distribution function (CDF). Equation (8) states that a high value of β corresponds to a high level of reliability. A variable's importance, or degree of contribution, to the reliability index from FORM can be determined by calculating its sensibility: $\mathrm{U}_i^*/|\mathbf{U}^*|$.

In this work, a Newton-Raphson type recursive algorithm developed by Rackwitz and Fiessler [31] is used to determine the MPP. The initial guess for the algorithm for each variable was chosen to be 0, corresponding to the mean of each variable in $\mathbf{Z}$-space.

2.3. Second Order Reliability Method (SORM)

Approximating the LSF using a linear surface, as is the case with FORM, will lead to a loss in accuracy if the LSF has a high level of curvature. The second-order reliability method (SORM) involves approximating the LSF using a second-order Taylor expansion and so is able to provide greater accuracy when used with non-linear LSFs, as is the case in this work with the BEM. In SORM, the LSF is approximated as:

$$g(\mathbf{U}) \approx g(\mathbf{U}^*) + \nabla g(\mathbf{U}^*)(\mathbf{U} - \mathbf{U}^*)^T + \frac{1}{2}(\mathbf{U} - \mathbf{U}^*)\mathbf{H}(\mathbf{U}^*)(\mathbf{U} - \mathbf{U}^*)^T \tag{9}$$

where $\mathbf{H}(\mathbf{U}^*)$ is the Hessian matrix evaluated at $\mathbf{U}^*$, and contains the second-order derivatives of the LSF with respect to the random variables in $\mathbf{U}$-space:

$$\mathbf{H}(\mathbf{U}^*) = \begin{bmatrix} \dfrac{\partial^2 g(\mathbf{U}^*)}{\partial \mathrm{U}_1^2} & \dfrac{\partial^2 g(\mathbf{U}^*)}{\partial \mathrm{U}_1 \partial \mathrm{U}_2} & \cdots & \dfrac{\partial^2 g(\mathbf{U}^*)}{\partial \mathrm{U}_1 \partial \mathrm{U}_q} \\ \dfrac{\partial^2 g(\mathbf{U}^*)}{\partial \mathrm{U}_2 \partial \mathrm{U}_1} & \dfrac{\partial^2 g(\mathbf{U}^*)}{\partial \mathrm{U}_2^2} & \cdots & \dfrac{\partial^2 g(\mathbf{U}^*)}{\partial \mathrm{U}_2 \partial \mathrm{U}_q} \\ \vdots & \vdots & \ddots & \vdots \\ \dfrac{\partial^2 g(\mathbf{U}^*)}{\partial \mathrm{U}_q \partial \mathrm{U}_1} & \dfrac{\partial^2 g(\mathbf{U}^*)}{\partial \mathrm{U}_q \partial \mathrm{U}_2} & \cdots & \dfrac{\partial^2 g(\mathbf{U}^*)}{\partial \mathrm{U}_q^2} \end{bmatrix} \tag{10}$$

Since SORM is of a higher-order than FORM it is expected that it will more accurately approximate non-linear LSFs, such as those involved in this work. The SORM used in this work is Breitung's asymptotic approximation [32]:

$$P_F = P\{g(\mathbf{Z}) < 0\} = \Phi(-\beta_{FORM}) \prod_{i=1}^{q-1} (1 + \beta_{FORM}\kappa_i)^{-1/2} \tag{11}$$

where β_{FORM} is the converged value of the reliability index calculated from FORM, and κ_i $(i = 1, \ldots, q-1)$ are the principal curvatures of the limit state function at the converged MPP location $\mathbf{U}^*$ from FORM. This approximation is accurate only for large values of β, which is the case for practical high-reliability problems [3, 33]. The probability of failure from SORM can now be calculated using equation (11) and the reliability index calculated using the following equation:

$$\beta = -\Phi^{-1}(P_F) = -\Phi^{-1}(1 - P_R) \tag{12}$$

2.4. Derivative evaluation

FORM and SORM both require the evaluation of the derivatives of the limit state function seen in equation (1). There are two methods that can be used to obtain these derivatives, these are the FDM, which involves the use of finite differences to approximate the derivatives, and the IDM, which involves the direct differentiation of the discretized boundary integral equations. In this work, the IDM is used to calculate the derivatives with respect to geometric random variables, while the FDM has been employed for variables such as applied load and Poisson's ratio.

2.4.1. Implicit Differentiation Method (IDM)

The IDM used in this work involves the direct differentiation of the boundary integral equations with respect to some geometric random variable Z_m $(m = 1, 2, \ldots, q-1)$. For conciseness, only the most important formulations related to the IDM are presented. The reader is referred to [16] for a comprehensive overview of the IDM used in this work as well as of the standard 2D elastostatic BEM formulations.

The 2D elastostatics displacement boundary integral equation is:

$$C_{ij}(\mathbf{x}')u_j(\mathbf{x}') + \fint_S T_{ij}(\mathbf{x}', \mathbf{x})u_j(\mathbf{x})dS = \int_S U_{ij}(\mathbf{x}', \mathbf{x})t_j(\mathbf{x})dS \tag{13}$$

where $\fint$ represents a Cauchy principal value integral. Subscripts i and j represent the dimensions of the problem, with $i, j = 1, 2$ for 2D problems. $\mathbf{x}'$ and $\mathbf{x}$ denote the collocation node and field point respectively. C_{ij} is the free term. $u_j(\mathbf{x}')$ and $t_j(\mathbf{x}')$ are the displacements and tractions respectively in the j'th direction at the collocation node $\mathbf{x}'$. This equation describes the displacements and tractions along each of the elements of the BEM model. The displacement and traction fundamental solutions for 2D elastostatics, U_{ij} and T_{ij} respectively, are:

$$U_{ij}(\mathbf{x}', \mathbf{x}) = \frac{1+\nu}{4\pi E(1-\nu)} \left\{ (3-4\nu) \ln\left(\frac{1}{r}\right) \delta_{ij} + r_{,i} r_{,j} \right\} \tag{14}$$

$$T_{ij}(\mathbf{x}', \mathbf{x}) = \frac{-1}{4\pi(1-\nu)r} \left\{ \frac{\partial r}{\partial n} [(1-2\nu)\delta_{ij} + 2r_{,i}r_{,j}] - (1-2\nu)(r_{,i}n_j - r_{,j}n_i) \right\} \tag{15}$$

where r is the distance between the collocation point $\mathbf{x}'$ and the field point $\mathbf{x}$, and $\partial r/\partial n = r_{,k}n_k = r_{,1}n_1 + r_{,2}n_2$. n_1 and n_2 are the components of the unit outward normal vector of the element which contains the field point (the field/integration element).

The discretized form of the 2D elastostatics displacement boundary integral equation (13) is:

$$C_{ij}(\mathbf{x}')u_j(\mathbf{x}') + \sum_{n_e=1}^{N_e} \sum_{\alpha=1}^{M} P_{ij}^{n_e\alpha} u_j^{n_e\alpha} = \sum_{n_e=1}^{N_e} \sum_{\alpha=1}^{M} Q_{ij}^{n_e\alpha} t_j^{n_e\alpha} \tag{16}$$

where the superscripts n_e and α denote field element number and local node number respectively, N_e is the total number of elements present in the BEM model, and M is the number of nodes in each element (3 for quadratic elements). For 2D problems:

$$P_{ij}^{n_e\alpha} = \fint_{-1}^{+1} T_{ij}(\mathbf{x}', \mathbf{x}(\eta)) N_\alpha(\eta) J^{n_e}(\eta) d\eta \tag{17}$$

$$Q_{ij}^{n_e\alpha} = \int_{-1}^{+1} U_{ij}(\mathbf{x}', \mathbf{x}(\eta)) N_\alpha(\eta) J^{n_e}(\eta) d\eta \tag{18}$$

where U_{ij} and T_{ij} are the 2D elastostatic displacement and traction fundamental solutions respectively, $N_\alpha(\eta)$ are the shape functions, defined in terms of the non-dimensional coordinate η ($-1 \le \eta \le 1$), and $J^{n_e}(\eta)$ is the Jacobian. The evaluation of (16) results in the following system of equations:

$$\mathbf{Hu} = \mathbf{Gt} \tag{19}$$

After the substitution of the known boundary conditions, the resulting system of equations is:

$$\mathbf{AX} = \mathbf{F} \tag{20}$$

where $\mathbf{A}$ is a matrix containing known coefficients, $\mathbf{X}$ is a vector of unknown boundary conditions, and $\mathbf{F}$ is a vector containing known coefficients and prescribed boundary conditions.

To obtain the first order derivatives of the boundary stresses necessary for FORM, the first-order derivative of equation (16) with respect to some geometric variable Z_m is required:

$$\begin{aligned} C_{ij,m}(\mathbf{x}')u_j(\mathbf{x}') + C_{ij}(\mathbf{x}')u_{j,m}(\mathbf{x}') + \sum_{n_e=1}^{N_e} \sum_{\alpha=1}^{M} P_{ij}^{n_e\alpha} u_{j,m}^{n_e\alpha} + \sum_{n_e=1}^{N_e} \sum_{\alpha=1}^{M} P_{ij,m}^{n_e\alpha} u_j^{n_e\alpha} \\ = \sum_{n_e=1}^{N_e} \sum_{\alpha=1}^{M} Q_{ij}^{n_e\alpha} t_{j,m}^{n_e\alpha} + \sum_{n_e=1}^{N_e} \sum_{\alpha=1}^{M} Q_{ij,m}^{n_e\alpha} t_j^{n_e\alpha} \end{aligned} \tag{21}$$

where $P_{ij}^{n_e\alpha}$ and $Q_{ij}^{n_e\alpha}$ were obtained from the normal BEM analysis (equations 17 and 18). Their derivatives with respect to Z_m are:

$$P_{ij,m}^{n_e\alpha} = \fint_{-1}^{+1} T_{ij,m}(\mathbf{x}', \mathbf{x}(\eta)) N_\alpha(\eta) J^{n_e}(\eta) d\eta + \fint_{-1}^{+1} T_{ij}(\mathbf{x}', \mathbf{x}(\eta)) N_\alpha(\eta) J_{,m}^{n_e}(\eta) d\eta \tag{22}$$

$$Q_{ij,m}^{n_e\alpha} = \int_{-1}^{+1} U_{ij,m}(\mathbf{x}', \mathbf{x}(\eta)) N_\alpha(\eta) J^{n_e}(\eta) d\eta + \int_{-1}^{+1} U_{ij}(\mathbf{x}', \mathbf{x}(\eta)) N_\alpha(\eta) J_{,m}^{n_e}(\eta) d\eta \tag{23}$$

Full expressions for the derivatives in (22) and (23) can be seen in the appendix. These derivatives contain the terms $r_{i,m} = \partial r_i / \partial \mathrm{Z}_m = [x_{i,m}(\mathbf{x}) - x_{i,m}(\mathbf{x}')]$ and $r_{,m} = r_{,k} r_{k,m}$, where $x_{i,m}$ is a function of the local node coordinates:

$$x_{i,m}(\eta) = \sum_{\alpha=1}^{M} N_\alpha(\eta) x_{i,m}^{\alpha} \tag{24}$$

In this work, $x_{i,m}^{\alpha}$ was calculated using the first-order finite difference scheme:

$$x_{i,m}^{\alpha} = \frac{x_i^{\alpha}(\mathrm{Z}_m + \Delta \mathrm{Z}_m') - x_i^{\alpha}(\mathrm{Z}_m)}{\Delta \mathrm{Z}_m'} \tag{25}$$

where $\Delta \mathrm{Z}_m'$ is a very small change in Z_m. It was found that the value of $\Delta \mathrm{Z}_m'$ made very little impact on the accuracy of the first-order derivatives from the IDM for all of the geometric variables Z_m investigated. $\Delta \mathrm{Z}_m'$ was given a normalised value equal to $1 \times 10^{-3}\%$ of Z_m as this was found to provide accurate results.

The IDM uses finite difference equations only for the calculation of $x_{i,m}^{\alpha}$, and later for $x_{i,mm}^{\alpha}$. After this, only the direct derivatives of the BEM integral equations are used.

From (21) the system of equations obtained is of the form:

$$\mathbf{H}_{,m}\mathbf{u} + \mathbf{H}\mathbf{u}_{,m} = \mathbf{G}_{,m}\mathbf{t} + \mathbf{G}\mathbf{t}_{,m} \tag{26}$$

Since the prescribed boundary conditions are constant, it is assumed that they will not change with a change in Z_m. It can therefore be said that if $u_j(\mathbf{x})$ is prescribed then $u_{j,m}(\mathbf{x}) = 0$, where $\mathbf{x}$ is a boundary node, the same is true for $t_j(\mathbf{x})$. After taking into account these prescribed boundary conditions the resulting system of equations is:

$$\mathbf{A}\mathbf{X}_{,m} = \mathbf{F}_{,m} - \mathbf{A}_{,m}\mathbf{X} \tag{27}$$

where $\mathbf{X}_{,m}$ contains the first order derivatives of the unknown boundary conditions. The matrices $\mathbf{A}$ and $\mathbf{X}$ are identical to those shown in (20) for the standard BEM analysis.

In the IDM, the entries of the matrix $\mathbf{A}_{,m}$ which correspond to the situation where both the collocation node and the integration element lie on fixed boundaries are zero. This occurs if a change in the geometric variable Z_m results in no change to either the x coordinate or the y coordinate of the collocation node or to any of the coordinates of any of the nodes in the integration element. This corresponds to the case where $x_{i,m}^{\alpha} = 0$ for all α and i for the integration element and $x_{i,m}^{c} = 0$ for all i, where c denotes the local node corresponding to the collocation node in the collocation node-containing element. Because of this, only the integration element - collocation node pairs which do not lie on fixed boundaries are required to be calculated. This significantly improves the computational efficiency of the above formulations.

To obtain the second order derivatives of the boundary stresses necessary for SORM, the second-order derivative of equation (16) with respect to some geometric variable Z_m are required:

$$\begin{aligned} & C_{ij,mm}(\mathbf{x}')u_j(\mathbf{x}') + 2C_{ij,m}(\mathbf{x}')u_{j,m}(\mathbf{x}') + C_{ij}(\mathbf{x}')u_{j,mm}(\mathbf{x}') \\ & + \sum_{n_e=1}^{N_e}\sum_{\alpha=1}^{M} P_{ij}^{n_e\alpha} u_{j,mm}^{n_e\alpha} + 2\sum_{n_e=1}^{N_e}\sum_{\alpha=1}^{M} P_{ij,m}^{n_e\alpha} u_{j,m}^{n_e\alpha} + \sum_{n_e=1}^{N_e}\sum_{\alpha=1}^{M} P_{ij,mm}^{n_e\alpha} u_{j}^{n_e\alpha} \\ & = \sum_{n_e=1}^{N_e}\sum_{\alpha=1}^{M} Q_{ij}^{n_e\alpha} t_{j,mm}^{n_e\alpha} + 2\sum_{n_e=1}^{N_e}\sum_{\alpha=1}^{M} Q_{ij,m}^{n_e\alpha} t_{j,m}^{n_e\alpha} + \sum_{n_e=1}^{N_e}\sum_{\alpha=1}^{M} Q_{ij,mm}^{n_e\alpha} t_{j}^{n_e\alpha} \end{aligned} \tag{28}$$

where $P_{ij,mm}^{n_e\alpha}$ and $Q_{ij,mm}^{n_e\alpha}$ are:

$$\begin{aligned} P_{ij,mm}^{n_e\alpha} &= \fint_{-1}^{+1} T_{ij,mm}(\mathbf{x}', \mathbf{x}(\eta))N_\alpha(\eta)J^{n_e}(\eta)d\eta \\ &+ 2\fint_{-1}^{+1} T_{ij,m}(\mathbf{x}', \mathbf{x}(\eta))N_\alpha(\eta)J_{,m}^{n_e}(\eta)d\eta + \fint_{-1}^{+1} T_{ij}(\mathbf{x}', \mathbf{x}(\eta))N_\alpha(\eta)J_{,mm}^{n_e}(\eta)d\eta \end{aligned} \tag{29}$$

$$\begin{aligned} Q_{ij,mm}^{n_e\alpha} &= \int_{-1}^{+1} U_{ij,mm}(\mathbf{x}', \mathbf{x}(\eta))N_\alpha(\eta)J^{n_e}(\eta)d\eta \\ &+ 2\int_{-1}^{+1} U_{ij,m}(\mathbf{x}', \mathbf{x}(\eta))N_\alpha(\eta)J_{,m}^{n_e}(\eta)d\eta + \int_{-1}^{+1} U_{ij}(\mathbf{x}', \mathbf{x}(\eta))N_\alpha(\eta)J_{,mm}^{n_e}(\eta)d\eta \end{aligned} \tag{30}$$

where $r_{i,mm} = \partial^2 r_i/\partial \mathrm{Z}_m^2 = x_{i,mm}(\mathbf{x}) - x_{i,mm}(\mathbf{x}')$, $r_{,mm} = r_{,im}r_{i,m} + r_{,i}r_{i,mm}$, and $r_{,im} = (r_{i,m} - r_{,i}r_{,m})/r$. $x_{i,mm}$ is a function of the local node coordinates:

$$x_{i,mm} = \sum_{\alpha=1}^{M} N_\alpha(\eta)x_{i,mm}^\alpha \tag{31}$$

In this work $x_{i,mm}$ was calculated using the second-order central finite difference scheme:

$$x_{i,mm}^\alpha = \frac{x_i^\alpha(\mathrm{Z}_m + \Delta\mathrm{Z}_m'') - 2x_i^\alpha(\mathrm{Z}_m) + x_i^\alpha(\mathrm{Z}_m - \Delta\mathrm{Z}_m'')}{(\Delta\mathrm{Z}_m'')^2} \tag{32}$$

where $\Delta\mathrm{Z}_m''$ is a very small change in Z_m. As with $\Delta\mathrm{Z}_m'$, it was found that the value of $\Delta\mathrm{Z}_m''$ made very little impact on the accuracy of the second-order derivatives obtained from the IDM for all of the geometric variables Z_m investigated. $\Delta\mathrm{Z}_m''$ was given a normalised value equal to 1% of Z_m as this was found to provide accurate results.

The system of equations resulting from (28) is of the form:

$$\mathbf{H}_{,mm}\mathbf{u} + 2\mathbf{H}_{,m}\mathbf{u}_{,m} + \mathbf{H}\mathbf{u}_{,mm} = \mathbf{G}_{,mm}\mathbf{t} + 2\mathbf{G}_{,m}\mathbf{t}_{,m} + \mathbf{G}\mathbf{t}_{,mm} \tag{33}$$

As before, it can be said that if $u_j(\mathbf{x})$ is prescribed then $u_{j,mm}(\mathbf{x}) = 0$, where $\mathbf{x}$ is a boundary node, the same is true for $t_j(\mathbf{x})$. After taking into account these prescribed boundary conditions the resulting system of equations is as follows:

$$\mathbf{A}\mathbf{X}_{,mm} = \mathbf{F}_{,mm} - 2\mathbf{A}_{,m}\mathbf{X}_{,m} - \mathbf{A}_{,mm}\mathbf{X} \tag{34}$$

where $\mathbf{X}_{,mm}$ contains the second order derivatives of the unknown boundary conditions. The matrices $\mathbf{A}$ and $\mathbf{X}$ are identical to those shown in (20) for the standard BEM analysis. $\mathbf{A}_{,m}$ and $\mathbf{X}_{,m}$ were obtained during the first-order derivative analysis using equation (27) and are used again here.

Similar to the first-order derivatives case, the entries of the matrix $\mathbf{A}_{,mm}$ which correspond to the situation where both the collocation node and the integration element lie on fixed boundaries are zero. This corresponds to the case where $x_{i,m}^\alpha = x_{i,mm}^\alpha = 0$ for all α and i for the integration element and $x_{i,m}^c = x_{i,mm}^c = 0$ for all i, where c denotes the local node corresponding to the collocation node in the collocation node-containing element. Because of this, only the integration element - collocation node pairs which do not lie on fixed boundaries are required to be calculated. This significantly improves the efficiency of the formulations.

Although the Hessian matrix $\mathbf{H}(\mathbf{U}^*)$ (equation 10) includes both diagonal terms and non-diagonal (cross-derivative) terms, it was found in this work that the presence of the cross-derivative terms produced only a very small change in β_{SORM} of, at most, 0.17%, while increasing the computation time of $\mathbf{H}(\mathbf{U}^*)$ by between 200%-1100%. Therefore, the non-diagonal terms in $\mathbf{H}(\mathbf{U}^*)$ were omitted.

Depending on the relative location of the collocation point $\mathbf{x}'$ and the field point $\mathbf{x}$, the integrals of the fundamental solutions seen in equations (17) and (18), (22) and (23), and (29) and (30) can be said to have one of five different levels of singularities. These levels go from regular integrals, which have no singularity and can be dealt with using standard Gaussian quadrature, to hyper-singular integrals, which are very strong singularities that have to be dealt with using special methods. Details on methods that can be used to deal with these five levels of singularities can be found in Chapter 11 of [16].

3. Multi-fidelity modelling

In this work, Kriging is used to create multi-fidelity models to approximate the response of a high-fidelity BEM model. Kriging models involve the use of design data in their creation. This design data is composed of the inputs to a BEM model, called the design sites, and the corresponding responses of the BEM model to these inputs. In this work, only one response is considered - the maximum stress in the structure, σ_A. The matrix of design sites, $\mathbf{S}$, and the vector of responses, $\mathbf{Y}$, are shown below:

$$\mathbf{S} = \begin{bmatrix} \mathbf{s}_1 \\ \mathbf{s}_2 \\ \vdots \\ \mathbf{s}_m \end{bmatrix} = \begin{bmatrix} s_{11} & s_{12} & \dots & s_{1n} \\ s_{21} & s_{22} & \dots & s_{2n} \\ \vdots & \vdots & \ddots & \vdots \\ s_{m1} & s_{m2} & \dots & s_{mn} \end{bmatrix} \tag{35}$$

$$\mathbf{Y} = \begin{bmatrix} y(\mathbf{s}_1) \\ y(\mathbf{s}_2) \\ \vdots \\ y(\mathbf{s}_m) \end{bmatrix} = \begin{bmatrix} Y_1 \\ Y_2 \\ \vdots \\ Y_m \end{bmatrix} \tag{36}$$

where m is the number of design sites, n is the number of input variables, and y is the response of the BEM model, σ_A.

The Design and Analysis of Computer Experiments (DACE) refers to methods used to determine the m design sites used in $\mathbf{S}$ to create the surrogate models. A common type of design used with DACE are Latin Hypercube designs, examples of which can be found in [6, 28, 27, 34]. Latin Hypercube (LHC) designs are widely used to create surrogate models for computer programs. LHC designs are space-filling and so provide good coverage over the design domain [34]. In this work, Latin Hypercube designs are used to obtain the design sites in $\mathbf{S}$.

The design points for each variable were determined by inversely uniformly sampling from the variable's cumulative distribution function (CDF). A number of intervals m were created between the probabilities 1% and 99% on each variable's CDF, and the median value for each interval was chosen, providing m equally-spaced values of probability between 1% and 99%. For each CDF, the inverse CDF for each of the m probabilities was then calculated, providing a total of m samples for each variable. By carrying out this procedure, a type of importance sampling is achieved. It is ensured that the design points are more concentrated in the more-likely areas of each variable's domain and less concentrated in the less-likely areas. An $m \times n$ matrix of design points can then be created and the order of the rows of each column can be randomized, ensuring that the data points cover the entire domain.

3.1. Kriging

Surrogate models created using Kriging are investigated in this work. Kriging involves the creation of a generalized least squares (GLS) model which accounts for the correlation in the residuals between the regression model and observations. Kriging is suitable for approximating computer models, which are deterministic in nature, since it interpolates the data points used to design the Kriging model [35]. In this work, Kriging is investigated for its ability to create accurate surrogate models of a BEM model for reliability analysis. The Matlab Kriging toolbox DACE [36] is used to create the Kriging models. For conciseness only a short introduction to Kriging is provided. More information on Kriging can be found in [37].

3.1.1. Mathematical form

A Kriging model is of the form:

$$\hat{y}(\mathbf{x}) = \mathbf{f}(\mathbf{x})^{\mathrm{T}}\boldsymbol{\beta} + z(\mathbf{x}) \tag{37}$$

where $\hat{y}(\mathbf{x})$ is termed the Kriging predictor and is the predicted output from the Kriging model at some trial site $\mathbf{x}$, where $x_j \in \mathbb{R}^n$. $\mathbf{f}(\mathbf{x})$ is a vector of length p containing the functions of the regression model evaluated at $\mathbf{x}$, where p is the number of parameters in the regression model. $\boldsymbol{\beta}$ is a vector of size p containing the regression coefficients. And $z(\mathbf{x})$ is a stationary Gaussian process with zero mean and covariance:

$$\mathrm{cov}[z(\mathbf{s}_i), z(\mathbf{x})] = \mathrm{E}[z(\mathbf{s}_i)z(\mathbf{x})] = \sigma^2\mathcal{R}(\boldsymbol{\theta}, \mathbf{s}_i, \mathbf{x}) \tag{38}$$

where E denotes expectation and σ^2 is the process variance. The correlation model or spatial correlation function (SCF) $\mathcal{R}$ controls the influence of nearby points on the output of the Kriging predictor $\hat{y}(\mathbf{x})$ by calculating the correlation between the design points $\mathbf{s}_i$, $i = (1, 2, \dots, m)$, and the trial site $\mathbf{x}$. The vector $\boldsymbol{\theta}$, $\theta_j \in \mathbb{R}^n$ $(\theta_j > 0)$, contains the parameters of the SCF and they determine the level of influence that the distance between the points $\mathbf{s}_i$ and $\mathbf{x}$ have on the correlation coefficient $\mathcal{R}$. The most commonly used SCF in engineering is the Gaussian correlation function, due to its ability to provide an approximation surface that is smooth and infinitely differentiable [37]. This is particularly useful in this work since the first-order and second-order derivatives of this surface are required by FORM and SORM. The Gaussian correlation function is therefore used in this work. It is of the following form:

$$\mathcal{R}(\boldsymbol{\theta}, \mathbf{s}_i, \mathbf{x}) = \prod_{j=1}^{n} \mathcal{R}_j(\theta_j, s_{ij}, x_j) = \prod_{j=1}^{n} \exp(-\theta_j|s_{ij} - x_j|^2) = \prod_{j=1}^{n} \exp(-\theta_j|d_j|^2) = \exp\left(\sum_{j=1}^{n}(-\theta_j|d_j|^2)\right) \tag{39}$$

3.2. Multi-fidelity modelling with the Boundary Element Method

In this work, two types of multi-fidelity models are used to approximate the maximum stress in the structure, σ_A. One type involves directly calling the low-fidelity BEM model each time a multi-fidelity approximation is required, the direct multi-fidelity models, and the other involves calling a surrogate model of the low-fidelity BEM model instead of the actual low-fidelity BEM model, these are the indirect multi-fidelity models. It is expected that the indirect models will be computationally less expensive than the direct models, but less accurate. In this work, calculating these multi-fidelity approximations involves creating correction Kriging models $\hat{\lambda}(\mathbf{x})$ and $\hat{\delta}(\mathbf{x})$. $\lambda(\mathbf{x})$ is the ratio between the maximum stress calculated from the high-fidelity BEM model $\sigma_A^{HF}(\mathbf{x})$ and the maximum stress calculated from the low-fidelity BEM model $\sigma_A^{LF}(\mathbf{x})$, while $\delta(\mathbf{x})$ is the difference between $\sigma_A^{HF}(\mathbf{x})$ and $\sigma_A^{LF}(\mathbf{x})$. The ratio and difference were used for the multi-fidelity approximations instead of derivative based approximations due to their ability to be applied to larger areas within the design domain and their ability to smooth out noise [27]. To create $\hat{\lambda}(\mathbf{x})$ and $\hat{\delta}(\mathbf{x})$, the ratio and the difference were calculated at each design point $\mathbf{s}_i$ $(i = 1, 2, \ldots, m)$ shown in equation (35):

$$\lambda(\mathbf{s}_i) = \frac{\sigma_A^{HF}(\mathbf{s}_i)}{\sigma_A^{LF}(\mathbf{s}_i)} \tag{40}$$

$$\delta(\mathbf{s}_i) = \sigma_A^{HF}(\mathbf{s}_i) - \sigma_A^{LF}(\mathbf{s}_i) \tag{41}$$

The vectors $\boldsymbol{\lambda}$ and $\boldsymbol{\delta}$ are used as $\mathbf{Y}$ in equation (36) for the creation of $\hat{\lambda}(\mathbf{x})$ and $\hat{\delta}(\mathbf{x})$ respectively. The multi-fidelity approximations for the maximum stress, σ_A, are as follows:

$$\hat{\sigma}_A^{MF1}(\mathbf{x}) = \hat{\lambda}(\mathbf{x})\sigma_A^{LF}(\mathbf{x}) \tag{42}$$

$$\hat{\sigma}_A^{MF2}(\mathbf{x}) = \hat{\delta}(\mathbf{x}) + \sigma_A^{LF}(\mathbf{x}) \tag{43}$$

$$\hat{\sigma}_A^{MF3}(\mathbf{x}) = \hat{\lambda}(\mathbf{x})\hat{\sigma}_A^{LF}(\mathbf{x}) \tag{44}$$

$$\hat{\sigma}_A^{MF4}(\mathbf{x}) = \hat{\delta}(\mathbf{x}) + \hat{\sigma}_A^{LF}(\mathbf{x}) \tag{45}$$

where $\hat{\sigma}_A^{LF}(\mathbf{x})$ is the surrogate Kriging model of the low-fidelity BEM model. Equations (42) and (43) correspond to the multi-fidelity approximations that involve directly calling the low-fidelity model, the direct multi-fidelity approximations, while equations (44) and (45) correspond to the multi-fidelity approximations that involve approximating the response of the low-fidelity model as a response surface, the indirect multi-fidelity approximations.

In addition to these multi-fidelity approximations, a surrogate model of the high-fidelity BEM model $\hat{\sigma}_A^{HF}(\mathbf{x})$, referred to as HFM*, was created and compared in terms of performance to the four multi-fidelity approximations above. The limit state functions of the four multi-fidelity models, the surrogate model of the high-fidelity BEM model, and the two BEM models can be seen below:

$$\hat{g}^{MFk}(\mathbf{Z}) = \sigma_c - \hat{\sigma}_A^{MFk}(\mathbf{X}) \qquad k = 1, 4 \tag{46}$$

$$\hat{g}^{HF}(\mathbf{Z}) = \sigma_c - \hat{\sigma}_A^{HF}(\mathbf{X}) \tag{47}$$

$$g^{LF}(\mathbf{Z}) = \sigma_c - \sigma_A^{LF}(\mathbf{X}) \tag{48}$$

$$g^{HF}(\mathbf{Z}) = \sigma_c - \sigma_A^{HF}(\mathbf{X}) \tag{49}$$

A flow diagram showing the steps involved in the creation of the Kriging models used for the multi-fidelity models can be seen in figure 1.

For FORM and SORM, the first and second-order derivatives of the limit state functions (equations 46 - 49) with respect to the variables in $\mathbf{Z}$ are required. Since the first-order derivatives of the limit state functions with respect to σ_c are equal to 1, it is more important to determine the derivatives with respect to the variables in $\mathbf{X}$. As an example, the first order derivative of $\hat{g}^{MF1}(\mathbf{Z})$ with respect to X_i $(i = 1, 2, ..., q-1)$ is:

$$\frac{\partial \hat{g}^{MF1}(\mathbf{Z})}{\partial X_i} = -\frac{\partial \hat{\sigma}_A^{MF1}(\mathbf{X})}{\partial X_i} = -\hat{\lambda}(\mathbf{X})\frac{\partial \sigma_A^{LF}(\mathbf{X})}{\partial X_i} - \sigma_A^{LF}(\mathbf{X})\frac{\partial \hat{\lambda}(\mathbf{X})}{\partial X_i} \tag{50}$$

The derivative $\partial\hat{\lambda}(\mathbf{X})/\partial X_i$ is the derivative of the response of the Kriging model $\hat{\lambda}$ and can be directly obtained. However, the derivative $\partial\sigma_A^{LF}(\mathbf{X})/\partial X_i$ is the derivative of the response of the low-fidelity BEM model and so is more difficult to obtain. It can be obtained using finite-differences with the FDM or directly with the IDM.

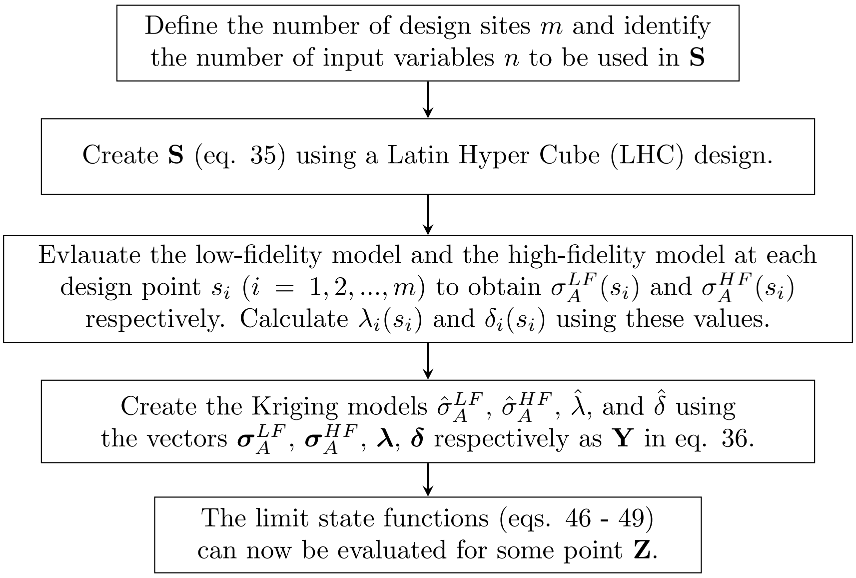

Figure 1: A flow diagram showing the steps involved in the creation of the Kriging models used for the multi-fidelity models.

4. Numerical examples

In this section, the proposed multi-fidelity modelling based structural reliability analysis formulations for the BEM with the IDM are validated for a pressurized thin ring structure for which the analytical solution is known. The application of the proposed methodology is also investigated for a more complex example featuring a I-beam section with a large number of random variables. Lastly, a significantly more complex example with a very low expected probability of failure (around $1 \times 10^{-4}\%$) is investigated to demonstrate the efficiency and robustness of the proposed IDM when used for reliability analysis with FORM and SORM. A part of this last example, a study is carried out to compare the computation time of FDM with the IDM.

4.1. Example 1: Thin ring

In order to validate the Boundary Element Method when calculating response derivatives using the IDM, a numerical example involving the thin ring structure shown in figure 2 subjected to uniform external pressure was investigated. The boundaries of the ring were discretised into 64 quadratic elements: 32 along the inner boundary, and 32 along the outer boundary. 64 elements were chosen as this number was found to provide stress convergence.

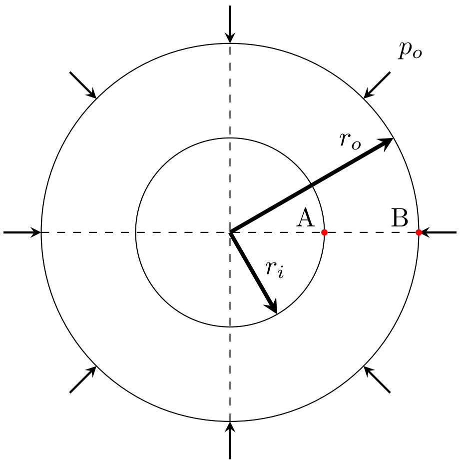

Figure 2: The pressurized thin ring used in example 1. Points A and B are labeled.

In this example the limit state function can be written as:

$$g(\mathbf{Z}) = \sigma_c - \sigma_A(\mathbf{X}) \tag{51}$$

where $\mathbf{Z} = (r_i, r_o, p_o, \sigma_c)$ and $\mathbf{X} = (r_i, r_o, p_o)$. σ_A is the value of maximum stress and occurs at point A in figure 1. The von Mises yield criterion is employed for the maximum stress:

$$\sigma_v(\mathbf{X})|_{\mathrm{A}} = \sigma_{vA}(\mathbf{X}) = \Big[\sigma_{11}^2(\mathbf{X})|_{\mathrm{A}} - \sigma_{11}(\mathbf{X})|_{\mathrm{A}}\sigma_{22}(\mathbf{X})|_{\mathrm{A}} + \sigma_{22}^2(\mathbf{X})|_{\mathrm{A}} + 3\sigma_{12}^2(\mathbf{X})|_{\mathrm{A}}\Big]^{1/2} \tag{52}$$

If $\sigma_{vA} > \sigma_c$, where σ_c is the yield strength, the structure is assumed to have failed. The analytical solution for σ_{vA} is expressed in terms of polar coordinates and can be found in [38].

The variables in $\mathbf{Z}$ were treated as random variables and were assigned the probability distributions seen in table 1. For simplicity, the variables were assigned non-dimensional values for the mean and coefficient of variation (COV), with COV $= \sigma/\mu$, where σ and μ are the standard deviation and mean respectively.

Z_i	X_i	Symbol	Description	Distribution	Mean	COV
Z_1	X_1	r_i	Inner radius	Lognormal	1.0	0.1
Z_2	X_2	r_o	Outer radius	Normal	10.0	0.1
Z_3	X_3	p_o	Outer pressure	Lognormal	1.0	0.2
Z_4	-	σ_c	Yield strength	Lognormal	3.0	0.2

Table 1: The four random variables investigated in example 1 and their probability distributions

4.1.1. Results and discussion

In order to validate the IDM, the first and second-order derivatives of the radial displacement u_r and the von Mises stress σ_v at points A and B in figure 1 with respect to the internal hole radius r_i were calculated using the IDM and compared to those obtained from the analytical solution. All displacements and stresses, as well as their derivatives, were calculated at the mean values of each variable shown in table 1. The BEM is able to approximate u_r and σ_v at both points A and B with a high level of accuracy, achieving percentage errors of the order of 1×10^{-4}%. This high level of accuracy is also seen in the first and second-order derivatives of u_r and σ_v shown in table 2.

	Model	
Derivative	Analytical	IDM
$\partial u_r(\mathrm{A})/\partial r_i$	-2.02039	-2.02037
$\partial u_r(\mathrm{B})/\partial r_i$	-3.98130×10^{-1}	-3.98128×10^{-1}
$\partial \sigma_v(\mathrm{A})/\partial r_i$	3.98130×10^{-2}	3.98127×10^{-2}
$\partial \sigma_v(\mathrm{B})/\partial r_i$	2.04948×10^{-2}	2.04947×10^{-2}
$\partial^2 u_r(\mathrm{A})/\partial r_i^2$	-1.21032×10^{-1}	-1.21030×10^{-1}
$\partial^2 u_r(\mathrm{B})/\partial r_i^2$	-4.16121×10^{-1}	-4.16118×10^{-1}
$\partial^2 \sigma_v(\mathrm{A})/\partial r_i^2$	4.16121×10^{-2}	4.16117×10^{-2}
$\partial^2 \sigma_v(\mathrm{B})/\partial r_i^2$	2.25971×10^{-2}	2.25969×10^{-2}

Table 2: First and second-order radial displacement derivatives $\partial u_r/\partial r_i$ and $\partial^2 u_r/\partial r_i^2$, and first and second-order von Mises stress derivatives $\partial \sigma_v/\partial r_i$ and $\partial^2 \sigma_v/\partial r_i^2$ evaluated at positions A and B using the analytical solution and the IDM.

It can be seen from table 2 that the IDM is able to accurately calculate the first-order and second-order derivatives of both the displacements and the boundary stresses at points A and B. Regarding the derivatives in table 2, it achieved a maximum percentage error with respect to the analytical solution of 1.7×10^{-3}%.

This demonstrates that the IDM approach used in this work can accurately calculate displacement and stress derivatives.

To further validate the IDM, the reliability indices, β, and probabilities of failure, P_F, calculated using FORM and SORM were compared to those obtained from the analytical solution. They are compared in table 3. The probability distributions seen in table 1 were used for each of the variables. The methodology shown in section 2 was used for FORM and SORM.

	β			P_F (%)		
Model	FORM	SORM	MCS	FORM	SORM	MCS
Analytical	1.41211	1.41073	1.410	7.8959	7.9162	7.927
IDM	1.41212	1.41075	-	7.8957	7.9160	-

Table 3: Reliability indices and probabilities of failure obtained from the analytical solution and the IDM using FORM, SORM, and MCS.

It can be seen from table 3 that the IDM provided very similar reliability indices to those obtained from the analytical solution, with percentage errors with respect to the analytical solution of $1.113\times10^{-3}\%$ and $1.110\times10^{-3}\%$ for FORM and SORM respectively. Reliability analyses were also carried out using MCS for the analytical solution. A reliability index of 1.410 and a probability of failure of 7.927% were obtained. A total of 3×10^{10} simulations were carried out to obtain convergence of the reliability index to 3 decimal places. The very small amount of error between SORM (for both the analytical solution and the IDM) and MCS for the analytical solution demonstrates the accuracy of SORM as well as of the IDM. Overall, the reliability indices obtained from FORM, SORM, and MCS are very similar, this is due to the simplicity of the example under investigation, with the variables in $\mathbf{X}$ showing highly linear relationships to σ_A over the domain investigated.

To explore the importance of each variable when evaluating the reliability indexes from FORM seen in Table 3, each variable's sensibility was calculated and they are shown in Table 4. It can be seen that the analytical solution and the IDM compare very well. The variables which contributed the most to the reliability indices were p_o and σ_c.

		Sensibility $U_i^*/\lvert\mathbf{U}^*\rvert$	
Notation	Symbol	Analytical	IDM
U_1	r_i	7.17747×10^{-3}	7.17743×10^{-3}
U_2	r_o	-7.20271×10^{-3}	-7.20268×10^{-3}
U_3	p_o	7.09569×10^{-1}	7.09569×10^{-1}
U_4	σ_c	-7.04563×10^{-1}	-7.04563×10^{-1}

Table 4: Sensibilities calculated for the analytical solution and the IDM for the variables in example 1.

Overall, results suggest that the IDM is able to accurately calculate the first-order and second-order derivatives of both boundary stresses and displacements. Validation of the IDM was accomplished through two approaches. The first approach involved comparing the derivatives calculated from the IDM to those obtained from an analytical solution, to which the IDM achieved very similar results. The second approach involved comparing the reliability indices obtained from FORM an SORM to those obtained using MCS, a method which does not require the calculation of derivatives. Results showed that the IDM was able to provide reliability indices for FORM and SORM that were very close to those obtained from MCS.

4.2. Example 2: I-beam section

In this example, the I-beam section with a center circular hole seen in figure 3 is considered. The limit state function in this case is:

$$g(\mathbf{Z}) = \sigma_c - \sigma_A(\mathbf{X}) \tag{53}$$

with $\mathbf{Z} = (t_{flange}, w_{flange}, t_{web}, l_{web}, r_{fillet}, r_{hole}, \sigma_{app}, \nu, \sigma_c)$ and $\mathbf{X} = (t_{flange}, w_{flange}, t_{web}, l_{web}, r_{fillet}, r_{hole}, \sigma_{app}, \nu)$. The random variables investigated and their probability distributions can be seen in table 5. Low COV values have been given to geometric variables since it is assumed that they can be measured quite accurately, while relatively high COV values have been given to the material properties and the applied load since they are typically more difficult to accurately measure than geometric variables. Also, the variation of the applied load and the material properties over the structure's service life will not be insignificant, adding uncertainty to their values.

The coefficient of variation of the applied stress (COV_{str}) was varied in the closed interval [0,0.2] in order to test the performance of the multi-fidelity models over a wide range of uncertainties. The coefficients of variation of the other variables were fixed. The I-beam is constructed out of steel ASTM-A36, the Poisson's ratio and tensile strength of which can be seen in table 5. The I-beam is subjected to uniform uniaxial tension along its flanges and is assumed to be under plane-strain conditions. The maximum stress occurs as a vertical stress, σ_{22}, at the edge of the center circular hole (point A in figure 3). Therefore, $\sigma_A = \sigma_{22}|_A$.

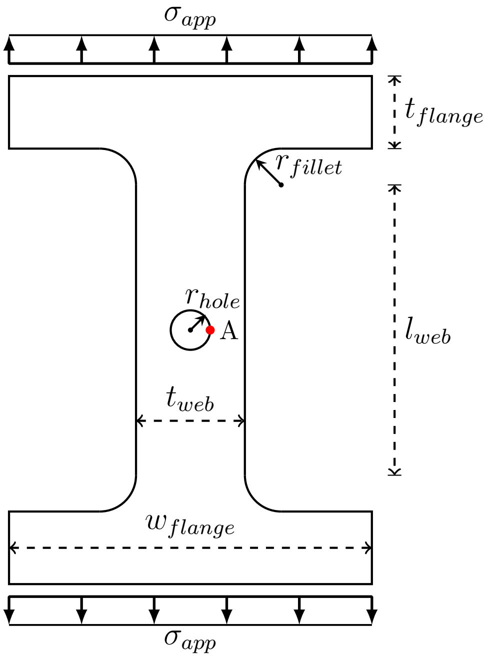

Figure 3: The I-beam section used in example 2

The boundaries of the I-beam seen in figure 3 were discretised into quadratic elements. Low-fidelity and high-fidelity BEM models of 30 and 120 elements respectively were created. The number of elements in the high-fidelity model was chosen based on a stress convergence test, while the number of elements in the low-fidelity model was arbitrarily chosen. The internal stress distribution for the low-fidelity and high-fidelity BEM models can be seen in figure 4. Around 4500 equally-space internal points were used for each model. It can be seen that the high-fidelity model provides a smoother distribution of stress throughout the structure.

Notation	Symbol	Description	Distribution	Mean	COV
Z_1	t_{flange}	Flange thickness	Normal	4.00 cm	0.05
Z_2	w_{flange}	Flange width	Lognormal	20.0 cm	0.05
Z_3	t_{web}	Web thickness	Lognormal	6.00 cm	0.05
Z_4	l_{web}	Web length	Normal	16.0 cm	0.05
Z_5	r_{fillet}	Fillet radius	Normal	2.00 cm	0.05
Z_6	r_{hole}	Hole radius	Lognormal	1.20 cm	0.05
Z_7	σ_{app}	Applied stress	Lognormal	13.0 MPa	$\mathrm{COV_{str}}$
Z_8	ν	Poisson's ratio	Normal	0.26	0.10
Z_9	$\sigma_c(\mathrm{T})$	Tensile strength	Lognormal	250 MPa	0.20

Table 5: The nine random variables investigated in example 2 and their probability distributions.

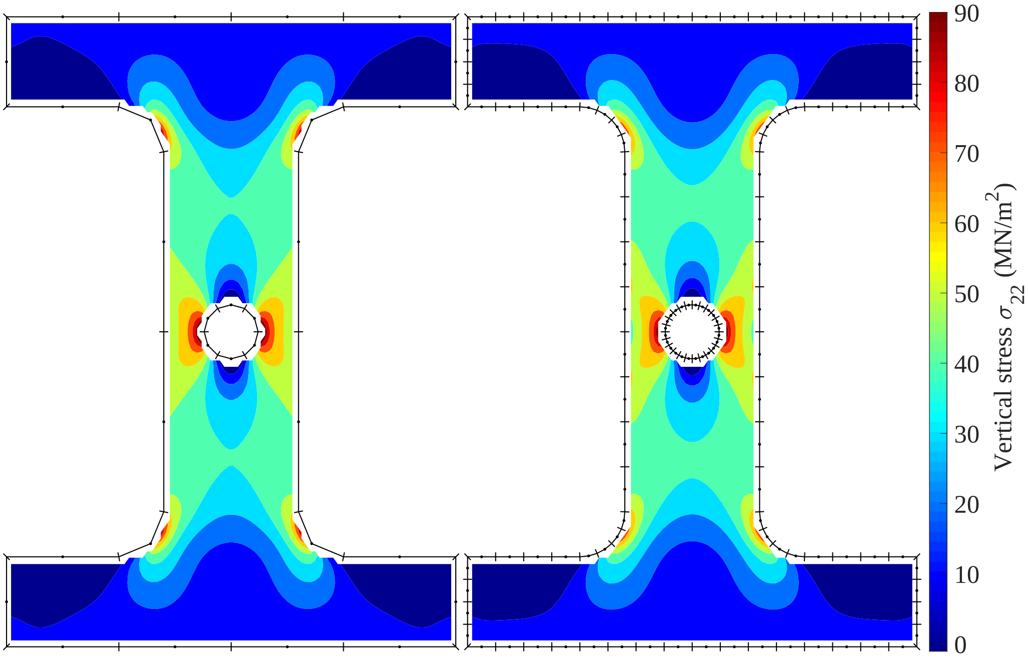

Figure 4: The low-fidelity model (left) and the high-fidelity model (right) used in example 2.

4.2.1. Multi-fidelity modelling

Kriging models with linear regression functions were created according to the method described in section 3. Two datasets were created for each Kriging model, a design dataset with 60 design points ($n_d = 60$), and a test dataset composed of 600 test points ($n_t = 600$). Since the coefficient of the variation $\mathrm{COV_{str}}$ is varied in the closed interval [0,0.2], the surrogate models were designed at $\mathrm{COV_{str}}$ to provide good coverage over the entire interval.

Table 6 shows various statistical parameters, R^2, R^2_{adj}, mean absolute percentage error (MAPE), and root mean squared error (RMSE), of the four Kriging models created using the above procedure when run with their test datasets. It is worth noting that since the Kriging models interpolate the design points, the Kriging model returns the exact responses at those points, making statistical parameters evaluated from the design dataset irrelevant. It can be seen that all of the surrogate models are highly accurate, with R^2 values of 0.98 or higher. Based on the MAPE and R^2 values, The ratio correction surface $\hat{\lambda}$ proved to be more accurate than the difference correction surface $\hat{\delta}$, suggesting that the multi-fidelity models based on $\hat{\lambda}$ could prove to be more accurate. Obtaining these four Kriging models using the above procedure required a CPU time of 310.3 minutes on a 6-core CPU. By parallelising key parts of the process, namely the creation of the response vector $\mathbf{Y}$, the total wall time was only 23.26 minutes.

Statistical parameter	$\hat{\lambda}(\mathbf{x})$	$\hat{\delta}(\mathbf{x})$	$\hat{\sigma}_A^{LF}(\mathbf{x})$	$\hat{\sigma}_A^{HF}(\mathbf{x})$
R^2	0.9985	0.9884	0.9989	0.9985
R^2_{adj}	0.9984	0.9882	0.9989	0.9985
MAPE (%)	1.81×10^{-2}	2.30	4.56×10^{-1}	3.32×10^{-1}
RMSE	3.57×10^{-4}	2.72×10^{1}	1.11×10^{2}	1.42×10^{2}

Table 6: Various statistical parameters evaluated using the test datasets for the four Kriging models.

To evaluate the performance of the resulting MFMs and the surrogate model of the HFM, they were used to calculate the maximum stress in the structure σ_A over 1×10^6 Monte Carlo simulations for the probability distributions shown in table 5. Several BEM models of various fidelities, including the LFM and the HFM, were also investigated. The results are shown in table 7. It can be seen that of the surrogate models, the direct MFMs proved to be the most accurate, obtaining MAPE values that were substantially less than the LFM, while requiring a very similar amount of CPU time to the LFM. On the other hand, the indirect MFMs and HFM* were significantly faster than the LFM, but were about 10 times less accurate than the direct MFMs.

Model type	Model	MAPE (%)	Average CPU time speed up ratio
Direct MFMs	MF1	2.0×10^{-2}	15.2
	MF2	9.4×10^{-2}	15.2
Indirect MFMs	MF3	4.7×10^{-1}	2.1×10^{4}
	MF4	4.8×10^{-1}	2.3×10^{4}
Surrogate model of the HFM	HFM*	3.8×10^{-1}	4.6×10^{4}
BEM models	E30 (LFM)	4.5	15.2
	E60	2.5	4.9
	E90	8.9×10^{-1}	2.1
	E120 (HFM)	0.00	1.0

Table 7: Mean absolute percentage error (MAPE) of the maximum stress σ_A calculated at the mean values of the variables shown in table 5 for each model. Also shown is the average CPU time speed up ratio for each model, compared to the HFM, evaluated over 1×10^6 runs. Notation 'EX' denotes a BEM model of 'X' elements.

4.2.2. Results and discussion

Reliability analyses were conducted with MCS, FORM, and SORM for values of COV_{str} in the closed interval [0,0.2] using the information shown in table 5. The results of these reliability analyses can be seen in figure 5. A total of 5×10^8 Monte Carlo simulations were carried out for each MCS datapoint for each of the seven models to ensure that the reliability indices converged to three decimal places. The results shown in figure 5 demonstrate that FORM and SORM are able to very reliably approximate the actual probability of failure given by MCS. The accuracy of SORM remains significantly higher than FORM for the values of COV_{str} investigated, this is due to the non-linearity of the limit state function and the fact that SORM uses a second-order Taylor expansion to approximate it. Despite this, the accuracy of SORM deteriorates slightly at higher levels of uncertainty, this is due to the increasing non-linearity of the limit state function.

It can also be seen from figure 5 that MF1 is highly accurate, closely matching the HFM for all three reliability analysis methods. It also proved to be the most accurate of the five surrogate models investigated, as can be seen from figure 6. It proved to be 2225, 1155, and 662, times more accurate than the LFM for FORM,

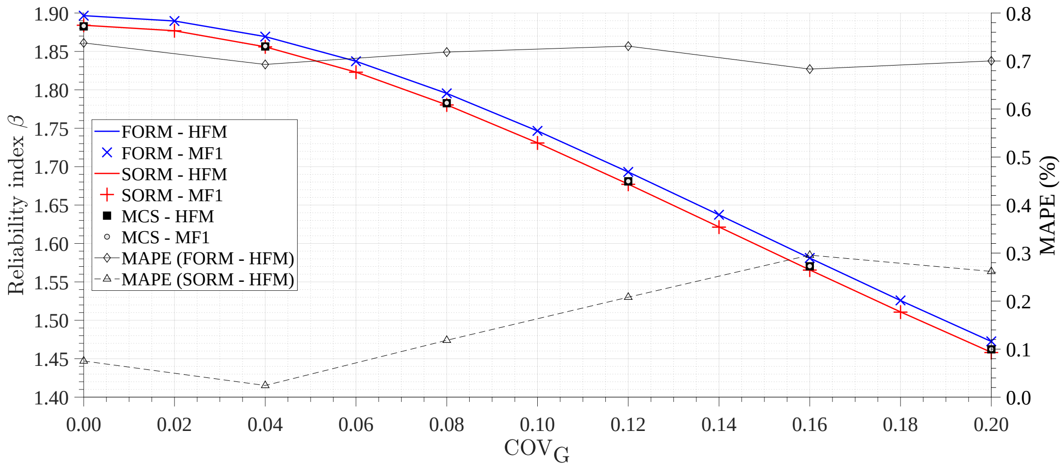

Figure 5: Reliability index β vs. the coefficient of variation of the applied stress $\mathrm{COV_{str}}$ for FORM, SORM, and MCS, for the HFM and MF1.

SORM, and MCS respectively. This suggests that the ratio-based MFMs are more accurate than the difference-based MFMs. Overall, the direct MFMs (MF1 and MF2), which involved directly calling the LFM, proved to be more accurate than the indirect MFMs (MF3 and MF4), which approximated the LFM as a surrogate model. The performance of the direct MFMs is made more notable when it is considered that the LFM has relatively large error of 4.5%, as can be seen from table 7. This is because it contains only one quarter of the elements present in the HFM. It is likely that increasing the number of elements in the LFM would improve the performance of the MFMs, at the expense of increased computation time. The surrogate model approximation of the HFM, HFM*, proved to be the least accurate out of all the surrogate models.

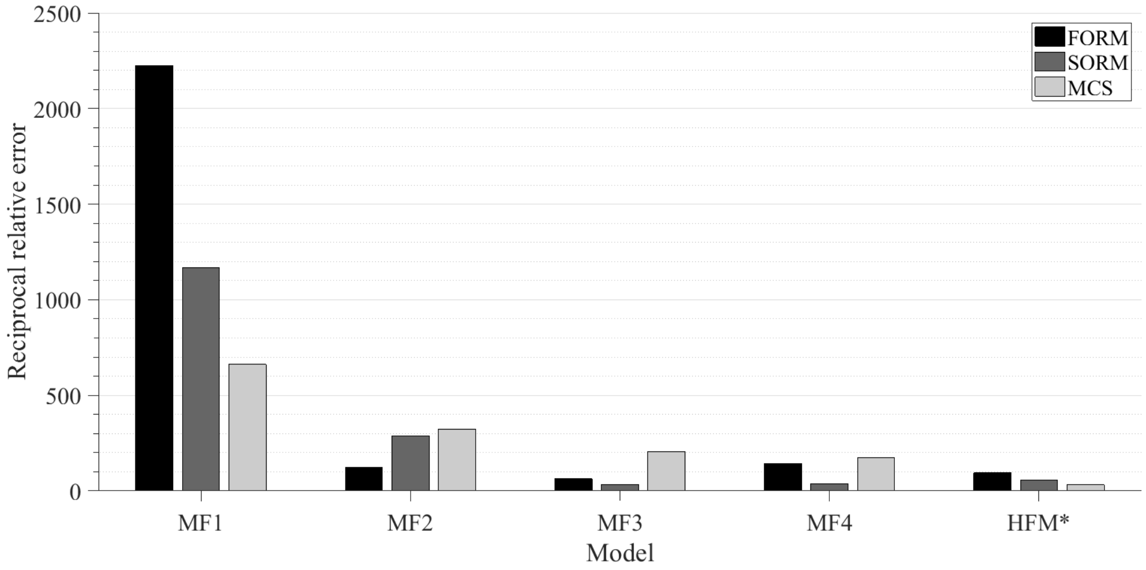

Figure 6: The reciprocal ratio of each model's average MAPE when calculating P_F to the average MAPE of the LFM for FORM, SORM, and MCS. The reciprocal relative error can be thought of as how many times smaller a model's error is compared to that of the LFM. For instance, the error of MF1 for FORM is about 2200 times smaller than that for the LFM.

From the first-order stress derivatives in table 8 it is clear that the direct MFMs are the most accurate, reflecting their good performance with FORM and SORM seen in figure 6. The comparatively worse performance of MF3, MF4, and HFM* for FORM and SORM is due to the fact that they are pure surrogate models with linear regression functions, therefore the first-order derivatives and second-order derivatives of their regression functions are constant and zero respectively. All of the surrogate models did a poor job in approximating the sensitivity for t_{flange}. This indicates that the relationship between t_{flange} and the maximum stress is highly non-linear. The linear regression functions used for the Kriging models in this example might not be able to accurately model this highly non-linear relationship. Therefore, higher-order regression functions might be more suitable in this case. The fact that it is the smallest sensitivity, and therefore difficult to accurately model, is also a factor.

	First-order derivative $\partial\sigma_A/\partial X_i$							
X_i	LFM	HFM	MF1	MF2	MF3	MF4	HFM*	Sensitivity units
t_{flange}	-11.9	-14.1	-8.5	-3.9	61.3	62.9	-78.0	kPa/cm
w_{flange}	750.7	797.9	798.1	799.6	792.8	794.6	810.6	MPa/cm
t_{web}	-3.3	-3.8	-3.8	-3.8	-3.7	-3.8	-3.8	GPa/cm
l_{web}	-70.5	-44.2	-45.8	-44.1	-57.2	-55.1	-41.0	kPa/cm
r_{fillet}	-1.5	-22.4	-20.7	-45.4	-36.3	-60.4	-14.5	kPa/cm
r_{hole}	4.9	6.4	6.4	6.4	7.0	7.0	6.6	GPa/cm
σ_{app}	11.9	12.5	12.5	12.5	12.4	12.5	12.4	-
ν	145.9	123.3	127.9	87.7	-197.3	-223.2	119.9	MPa

Table 8: First-order derivatives of σ_A with respect to the random variables in $\mathbf{X}$ for each of the seven models investigated. The derivatives are evaluated at the mean values shown in table 5.

To compliment the sensitivities seen in Table 8, the sensibility of each variable was calculated and is shown in Table 9. It can be seen that the FDM and the IDM compare very well. The most important variables were found to be σ_c, σ_{app}, and t_{web}. This compares well with the sensitivities seen in Table 8.

		Sensibility $U_i^*/\lvert\mathbf{U}^*\rvert$	
Notation	Symbol	FDM	IDM
U_1	t_{flange}	-6.08180×10^{-4}	-6.08184×10^{-4}
U_2	w_{flange}	2.09150×10^{-1}	2.09149×10^{-1}
U_3	t_{web}	-3.07861×10^{-1}	-3.07865×10^{-1}
U_4	l_{web}	-9.56888×10^{-3}	-9.56894×10^{-3}
U_5	r_{fillet}	-4.92136×10^{-4}	-4.92136×10^{-4}
U_6	r_{hole}	1.09372×10^{-1}	1.09371×10^{-1}
U_7	σ_{app}	4.16486×10^{-1}	4.16486×10^{-1}
U_8	ν	1.00179×10^{-3}	1.00179×10^{-3}
U_9	σ_c(T)	-8.22169×10^{-1}	-8.22169×10^{-1}

Table 9: Sensibilities calculated for the final iteration of FORM for the FDM and the IDM for the variables in example 2 using the HFM.

It is worth noting that the response of a Kriging model is composed of two parts, as can be seen in equation (37). Even though the second-order derivatives of the regression function $\mathbf{f}(\mathbf{x})^{\mathrm{T}}\boldsymbol{\beta}^*$ will equal zero in the case of it being linear, the second-order derivatives of the right-hand side $z(\mathbf{x})$ will be non-zero since the spatial correlation function (SCF) $\mathcal{R}$ used is Gaussian which is infinitely differentiable. Therefore, the second-order derivatives of the response of a Kriging model will be non-zero even if it has a linear regression function. If the Kriging model had been constructed with a regression function of a higher order, then it is likely that its derivatives would be more accurate.

It can be seen from figure 7 that the LFM was around 9-24 times faster in terms of CPU-time than the HFM for each of the three reliability analysis methods. Of the MFMs, the direct MFMs proved to be the slowest, with average CPU times 5% higher than the LFM across the three methods. The indirect MFMs were less accurate, but 80-700 times faster than the LFM. The indirect models show a great deal of potential to be used with MCS due to their low computational cost and good accuracy. Obtaining a reliability index from MCS for the HFM required, on average, a CPU time of 70 hours for 5×10^8 simulations. For MF3 or MF4 this was reduced to just 40 seconds with an average error of 0.08%, this reflects a significant improvement in efficiency. The surrogate model of the high-fidelity model, HFM*, proved to be the fastest model, but the least accurate. It proved to be 130-1400 times faster than the LFM. When used with MCS it could complete 2.5×10^8 simulations in 20 seconds with an average error of 0.3%, this is faster but less accurate than the indirect MFMs.

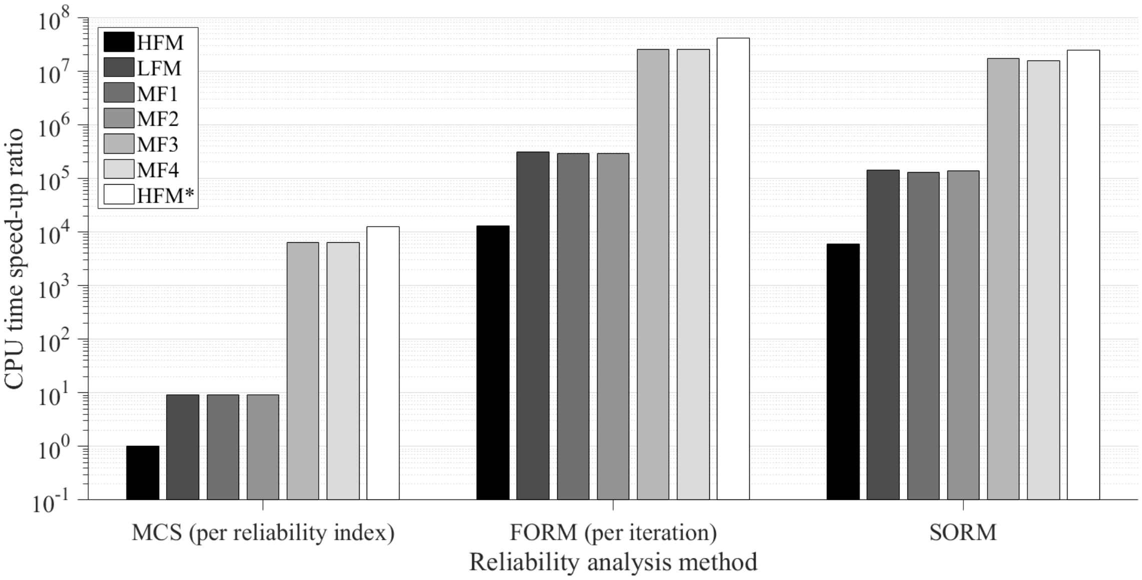

Figure 7: The CPU time speed-up ratio for each model to obtain a reliability index from FORM, SORM, and MCS. The reference CPU time is the CPU time required by the HFM for MCS. The times shown for SORM exclude the time for FORM.

Overall, the multi-fidelity models proved to be much more efficient than the HFM when run with FORM, SORM, and MCS. The multi-fidelity models were able to achieve similar levels of accuracy to the HFM, but with significantly less computational cost, even when there was a large disparity in terms of the number of elements between the low-fidelity and high-fidelity models. The IDM proved to be highly accurate when used with FORM and SORM, obtaining reliability indices that matched well with MCS.

4.3. Example 3: Triangular support bracket

To demonstrate the efficiency and robustness of the proposed IDM when used for reliability analysis with FORM and SORM, a significantly more complex example is investigated. For this example, a very low probability of failure (around 1×10^{-4}%) is expected. A study is also carried out to compare the computation time of FDM with the IDM.

In this example, the triangular support bracket seen in figure 8 is considered. The LSF in this case is:

$$g(\mathbf{Z}) = \sigma_c - \sigma_A(\mathbf{X}) \tag{54}$$

where $\mathbf{Z}=(h_1, h_2, w_1, w_2, l_1, l_2, t_1, t_2, r_1, r_2, r_3, r_4, r_5, \sigma_{app}, \nu, \sigma_c)$ and $\mathbf{X}=(h_1, h_2, w_1, w_2, l_1, l_2, t_1, t_2, r_1, r_2, r_3, r_4, r_5, \sigma_{app}, \nu)$, the definitions of which can be seen in Figure 8. The probability distributions of these variables can be seen in Table 10. The bracket is subjected to a compressive load along its top edge of magnitude σ_{app}, it is fixed to a wall on its left edge. The bracket is composed of steel ASTM-A36, the Poisson's ratio and compressive strength of which can be seen in Table 10. In this example, the von Mises yield criterion is used (equation 52).

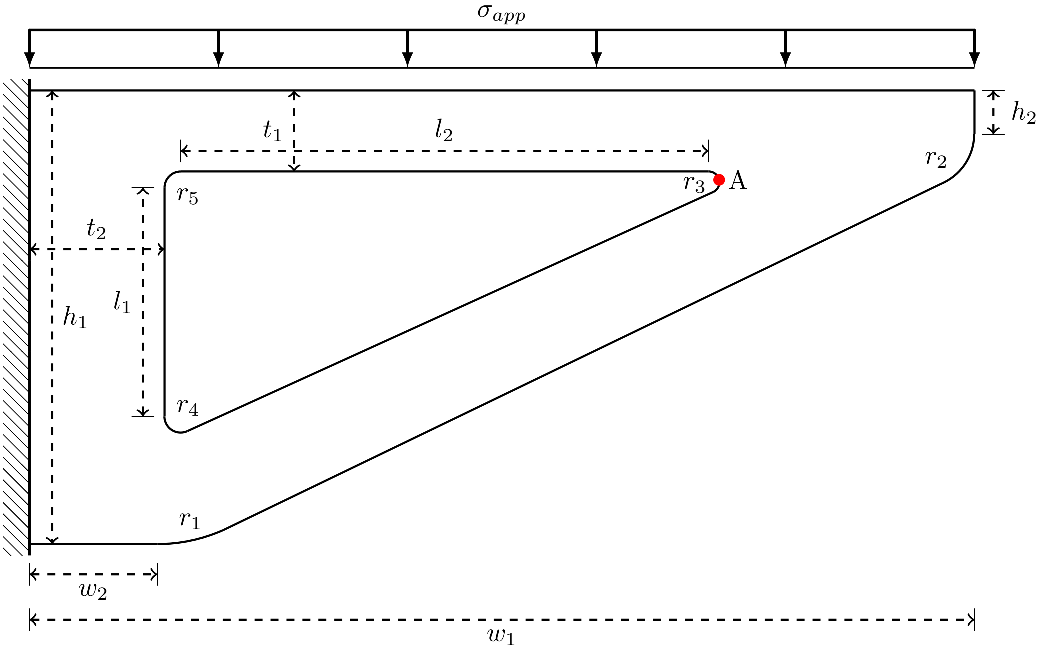

Figure 8: The triangular support used for example 3.

Notation	Symbol	Description	Probability distribution	Mean	Coefficient of variation
Z_1	h_1	See Figure 8	Normal	84 cm	0.05
Z_2	h_2	See Figure 8	Normal	20 cm	0.05
Z_3	w_1	See Figure 8	Lognormal	175 cm	0.05
Z_4	w_2	See Figure 8	Lognormal	30 cm	0.05
Z_5	l_1	See Figure 8	Normal	50 cm	0.05
Z_6	l_2	See Figure 8	Lognormal	110 cm	0.05
Z_7	t_1	See Figure 8	Normal	15 cm	0.05
Z_8	t_2	See Figure 8	Normal	25 cm	0.05
Z_9	r_1	See Figure 8	Lognormal	30 cm	0.05
Z_{10}	r_2	See Figure 8	Lognormal	10 cm	0.05
Z_{11}	r_3	See Figure 8	Normal	2 cm	0.05
Z_{12}	r_4	See Figure 8	Lognormal	3 cm	0.05
Z_{13}	r_5	See Figure 8	Lognormal	3 cm	0.05
Z_{14}	σ_{app}	Applied stress	Normal	700 kPa	0.2
Z_{15}	ν	Poisson's ratio	Normal	0.26	0.1
Z_{16}	σ_c(C)	Material strength	Lognormal	152 MPa	0.1

Table 10: The 16 variables investigated in example 3 and their probability distributions

The boundaries of the triangular support bracket were discretised into quadratic elements. A high-fidelity model of 80 elements was created. The number of elements in this model was determined in a similar manner as in section 4.2. All the analyses in this example were conducted with this high-fidelity model.

The reliability indices and probabilities of failure obtained from the FDM and the IDM for both FORM and SORM can be seen in Table 11. It can be seen that the FDM and the IDM compare very well with both FORM and SORM even though the probability of failure is very low. The difference between FDM and the IDM for FORM was about 1.2×10^{-5}%, while for SORM it was about 2.4×10^{-2}%. The greater difference between FORM and SORM in this example can be attributed to the fact that the triangular support bracket has a much more complex geometry when compared to the thin ring or the I-beam investigated previously, and so the limit state function is more non-linear.

	β		P_F ($\times 10^{-4}$ %)	
Model	FORM	SORM	FORM	SORM
FDM	4.712	4.742	1.228	1.060
IDM	4.712	4.743	1.228	1.054

Table 11: Reliability indices and probabilities of failure obtained from FDM and the IDM using FORM and SORM.

A study was carried out to determine the variables which contribute the most to the reliability indexes seen in Table 11 for FORM. To achieve this, each variable's sensibility $U_i/|\mathbf{U}|$ was calculated with FDM and the IDM. The results can be seen in Table 12. It can be seen that the sensibilities from FDM and IDM compare very well. The most important variables are σ_{app}, l_2, and σ_c.

		Sensibility $U_i^*/|\mathbf{U}^*|$	
Notation	Symbol	FDM	IDM
U_1	h_1	-3.46363×10^{-1}	-3.46372×10^{-1}
U_2	h_2	-3.54233×10^{-2}	-3.54226×10^{-2}
U_3	w_1	-9.01558×10^{-2}	-9.01491×10^{-2}
U_4	w_2	-3.22386×10^{-2}	-3.22389×10^{-2}
U_5	l_1	1.40243×10^{-1}	1.40244×10^{-1}
U_6	l_2	5.14653×10^{-1}	5.14654×10^{-1}
U_7	t_1	-1.31078×10^{-1}	-1.31075×10^{-1}
U_8	t_2	3.50662×10^{-2}	3.50666×10^{-2}
U_9	r_1	-1.03602×10^{-4}	-1.03613×10^{-4}
U_{10}	r_2	9.26508×10^{-3}	9.26509×10^{-3}
U_{11}	r_3	-8.05146×10^{-3}	-8.05147×10^{-3}
U_{12}	r_4	-9.19377×10^{-2}	-9.19378×10^{-2}
U_{13}	r_5	-1.29018×10^{-3}	-1.29022×10^{-3}
U_{14}	σ_{app}	5.89213×10^{-1}	5.89210×10^{-1}
U_{15}	ν	1.13206×10^{-3}	1.13206×10^{-3}
U_{16}	σ_c(C)	-4.59223×10^{-1}	-4.59221×10^{-1}

Table 12: Sensibilities calculated for the final iteration of FORM for the FDM and the IDM for the variables in example 3.

To compare the computation time of the FDM and the IDM, both the FDM and the IDM were used to calculate the reliability index for FORM and SORM for the triangular support bracket shown in Figure 8 with the variables seen in Table 10. This reliability index was calculated 200 times for each combination of FDM & IDM and FORM & SORM, and the average CPU time for each combination was calculated. The results can be seen in Table 13. It can be seen that the IDM requires about 0.30% and 1.32% more CPU time respectively for FORM and SORM on average than the FDM to calculate the reliability index. This indicates that, once the optimal stepsize for the FDM has been found, there is very little difference in the computation time between the FDM and the IDM when used to calculate the reliability index.

	CPU time (s)	
Model	FORM	SORM
FDM	82.55	92.35
IDM	82.30	91.15

Table 13: Average CPU time required by the FDM and the IDM when calculating the reliability index for the triangular support bracket with FORM and SORM. 200 runs were used to obtain the averages.

The main disadvantage of the FDM is that its accuracy is highly dependent on the stepsize used. Therefore, a trial-and-error approach is required to determine the optimal stepsize. This can be time-consuming, especially for complex problems. Although a finite-difference scheme is used at the very beginning of the IDM in order to obtain the sensitivities of the nodal coordinates, the stepsize in this case has very little influence on the accuracy of these nodal sensitivities. The IDM thereby avoids the need for a time-consuming trial-and-error approach. As a result, it is expected that the overall time required by the IDM, including set-up and use, is significantly less than that required by the FDM. This difference is expected to be magnified for more complex problems.

In this example, the stepsizes used for the FDM were normalised with respect to the variables in $\mathbf{X}$. A range of normalised stepsizes from 1×10^{-7} to 1×10^{-1} were investigated. The first-order and second-order derivatives of the limit state function with respect to the variables in $\mathbf{X}$ can be calculated for this range of stepsizes as part of the trial-and-error procedure. The derivatives are expected to be unstable for very low stepsizes and also for very high stepsizes due to rounding error and truncation error respectively. However, there will be a range of stepsizes for which the derivatives are stable. The optimal stepsize is chosen from this range. For this example, the optimal normalised stepsize for the first-order and second-order derivatives were found to be 1×10^{-5} and 1×10^{-2} respectively. These normalised stepsizes were found to be optimal for all of the variables in $\mathbf{X}$. However, this may not be true in all cases. On average, it was found that the minimum CPU time required to obtain the optimal stepsize for all the variables in this example was around 184.95 s for the first-order derivatives and 388.13 s for the second-order derivatives. These times do not include the set-up of the optimization procure nor the analysis of the derivatives, which can contribute greatly to the overall computation time. Given that these times are significantly larger than those shown in Table 13, and that optimal stepsizes should be recalculated when the value of a variable is changed significantly and when another structure is being investigated, the calculation of these optimal stepsizes can contribute significantly to the overall computation time associated with the reliability analysis of structures.

In conclusion, the proposed IDM methodology was shown to provide a much more efficient alternative to the FDM for the reliability analysis of complex structures. This is due to the fact that, unlike the FDM, the IDM avoids the need to conduct a time-consuming trial-and-error approach to determine the optimal stepsizes for the derivatives of the design variables.

5. Conclusions

In this work, a novel multi-fidelity modelling methodology for structural reliability analysis using the Boundary Element Method (BEM) with an Implicit Differentiation Method (IDM) is presented. The higher-order sensitivities of the elastostatic BEM equations to changes several geometric variables were derived for use with SORM with the IDM, and results were compared to those obtained from MCS and FORM. Multi-fidelity models in the form of Kriging models were created, and their performance, in terms of accuracy and computation time was compared.

Three numerical examples were investigated: 1) a thin ring subjected to external pressure, 2) an I-beam section, and 3) a triangular support bracket. Results from example 1 demonstrated the accuracy of the IDM in the calculation of boundary displacement and stress derivatives for a problem for which the analytical solution is known.

Example 2 featured the application of a variety of multi-fidelity models. Results showed that the direct multi-fidelity models, those directly calling the low-fidelity model, were significantly more accurate for FORM, SORM, and MCS than the Kriging surrogate model approximation of the high-fidelity model and the indirect models, those which approximated the low-fidelity model with a Kriging surrogate model. It was found that the direct models provided more accurate response derivatives than the indirect models, and so provided more accurate reliability indices when used with FORM and SORM. However, the indirect models and the Kriging surrogate model approximation of the high-fidelity model, while providing less accurate response derivatives, provided response values than were similar in accuracy to the direct models but with significantly less computational cost, they therefore proved superior when used for MCS. This suggests that for complex problems, direct models are best suited for use with FORM and SORM due to their ability to provide highly accurate response derivatives. Since FORM and SORM are relatively cheap compared to MCS, the benefit of using the indirect models for these methods is less clear. The indirect models proved to be best used with MCS, due to their ability to provide responses of similar accuracy to the direct models but with significantly less computational cost. All of the multi-fidelity models investigated offered a significant improvement in accuracy over the low-fidelity model.

As part of example 3 a study was carried out to compare the computation time of the FDM and the IDM for a complex structure with many design variables. It was found that the IDM provides a much more efficient alternative to the FDM for reliability analysis. This is because, unlike the FDM, the IDM avoids the need for a time-consuming stepsize optimization procedure.

Compared to the low-fidelity model, the multi-fidelity models were able to provide probabilities of failure that were up to 2225 times more accurate. And when compared to the high-fidelity model, they were able to provide computational costs that were over 6000 times less. This represents a reduction in the computational cost of MCS from 70 hours for the high-fidelity model to just 40 seconds for the indirect models with an average error of 0.08 %. This is a significant improvement in efficiency and demonstrates the potential of the proposed IDM/multi-fidelity modelling methodology for use in the reliability analysis of complex problems with many design variables under high levels of uncertainty.

Acknowledgments

This research was supported by a grant provided by the Engineering and Physical Sciences Research Council (EPSRC).

Appendix A. IDM formulations

The first order derivatives of the displacement and traction fundamental solutions (equations 14 & 15 respectively) are:

$$U_{ij,m} = \frac{1+\nu}{4\pi E(1-\nu)r}\Big[(r_{i,m}r_{,j} + r_{j,m}r_{,i}) - ((3-4\nu)\delta_{ij} + 2r_{,i}r_{,j})r_{,m}\Big] \tag{A.1}$$

$$\begin{aligned} T_{ij,m} =& \frac{-1}{4\pi(1-\nu)r^2}\Bigg[2\frac{\partial r}{\partial n}\{r_{i,m}r_{,j} + r_{j,m}r_{,i} - ((1-2\nu)\delta_{ij} + 4r_{,i}r_{,j})r_{,m}\} + (n_k r_k)_{,m}((1-2\nu)\delta_{ij} \\ & + 2r_{,i}r_{,j}) + (1-2\nu)(n_{i,m}r_j - n_{j,m}r_i + n_i r_{j,m} - n_j r_{i,m}) - 2(1-2\nu)(n_i r_{,j} - n_j r_{,i})r_{,m}\Bigg] \end{aligned} \tag{A.2}$$

The second order derivatives are:

$$\begin{aligned} U_{ij,mm} =& \frac{1+\nu}{4\pi E(1-\nu)r^2}\Big[(3-4\nu)(r_{,m}^2 - r_{,mm}r)\delta_{ij} + (6r_{,m}^2 - 2r_{,mm}r)r_{,i}r_{,j} \\ & + (r_{i,mm}r_j + 2r_{i,m}r_{j,m} + r_i r_{j,mm}) - 4(r_{i,m}r_{,j} + r_{,i}r_{j,m})r_{,m}\Big] \end{aligned} \tag{A.3}$$

$$
\begin{aligned}
T_{ij,mm} = {} & \frac{-1}{4\pi(1-\nu)r^3}\Bigg[2(\frac{\partial r}{\partial n})_{,m}[r_{i,m}r_{,j} + r_{j,m}r_{,i} - ((1-2\nu)\delta_{ij} + 4r_{,i}r_{,j})r_{,m}] \\
& + 2\frac{\partial r}{\partial n}[r_{i,mm}r_{,j} + 2r_{i,m}r_{j,m} + r_{,i}r_{j,mm} - ((1-2\nu)\delta_{ij} + 4r_{,i}r_{,j})r_{,mm}r \\
& - (4r_{i,m}r_j + 4r_i r_{j,m})r_{,m}r - 2r_{i,m}r_{,j}r_{,m} - 2r_{,i}r_{j,m}r_{,m} + 2((1-2\nu)\delta_{ij} + 4r_{,i}r_{,j})r_{,m}^2] \\
& + (r_k n_k)_{,mm}[(1-2\nu)\delta_{ij} + 2r_{,i}r_{,j}] + 2(r_k n_k)_{,m}(r_{,im}r_{,j} + r_{,i}r_{,jm}) \\
& + (1-2\nu)(r_{j,mm}n_i + 2r_{j,m}n_{i,m} + r_j n_{i,mm} - r_{i,mm}n_j - 2r_{i,m}n_{j,m} - r_i n_{j,mm} \\
& + 2(1-2\nu)[(n_j r_{,i} - n_i r_{,j})r_{,mm} + (n_j r_{,im} + n_{j,m}r_{,i} - n_{i,m}r_{,j}n_i r_{,jm})r_{,m}\Bigg]
\end{aligned}
\tag{A.4}
$$

The Jacobian is:

$$
J^{n_e}(\eta) = \left[\left(\frac{dx_1(\eta)}{d\eta}\right)^2 + \left(\frac{dx_2(\eta)}{d\eta}\right)^2\right]^{1/2}
\tag{A.5}
$$

The first order derivative is:

$$
J^{n_e}_{,m}(\eta) = \frac{1}{J^{n_e}(\eta)}\left[\frac{dx_1(\eta)}{d\eta}\frac{dx_{1,m}(\eta)}{d\eta} + \frac{dx_2(\eta)}{d\eta}\frac{dx_{2,m}(\eta)}{d\eta}\right]
\tag{A.6}
$$

The second order derivative is:

$$
\begin{aligned}
J^{n_e}_{,mm}(\eta) = {} & \frac{1}{J^{n_e}(\eta)}\left[\left(\frac{dx_{1,m}(\eta)}{d\eta}\right)^2 + \left(\frac{dx_{2,m}(\eta)}{d\eta}\right)^2 + \frac{dx_1(\eta)}{d\eta}\frac{dx_{1,mm}(\eta)}{d\eta} + \frac{dx_2(\eta)}{d\eta}\frac{dx_{2,mm}(\eta)}{d\eta}\right] \\
& - \frac{1}{J^{n_e}(\eta)^3}\left[\frac{dx_1(\eta)}{d\eta}\frac{dx_{1,m}(\eta)}{d\eta} + \frac{dx_2(\eta)}{d\eta}\frac{dx_{2,m}(\eta)}{d\eta}\right]^2
\end{aligned}
\tag{A.7}
$$

The components of the unit outward normal vector are:

$$
n_1(\eta) = \frac{1}{J^{n_e}(\eta)}\frac{dx_2(\eta)}{d\eta}
\tag{A.8}
$$

$$
n_2(\eta) = -\frac{1}{J^{n_e}(\eta)}\frac{dx_1(\eta)}{d\eta}
\tag{A.9}
$$

The first order derivatives are:

$$
n_{1,m}(\eta) = \frac{1}{J^{n_e}(\eta)}\left[\frac{dx_{2,m}(\eta)}{d\eta} - n_1(\eta)J^{n_e}_{,m}(\eta)\right]
\tag{A.10}
$$

$$
n_{2,m}(\eta) = -\frac{1}{J^{n_e}(\eta)}\left[\frac{dx_{1,m}(\eta)}{d\eta} - n_2(\eta)J^{n_e}_{,m}(\eta)\right]
\tag{A.11}
$$

The second order derivatives are:

$$
\begin{aligned}
n_{1,mm}(\eta) = {} & \frac{1}{J^{n_e}(\eta)}\frac{dx_{2,mm}(\eta)}{d\eta} - \frac{1}{(J^{n_e}(\eta))^2}\Bigg[2J^{n_e}_{,m}(\eta)\frac{dx_{2,m}(\eta)}{d\eta} \\
& + J^{n_e}_{,mm}(\eta)\frac{dx_2(\eta)}{d\eta}\Bigg] + 2\frac{(J^{n_e}_{,m}(\eta))^2}{(J^{n_e}(\eta))^3}\frac{dx_2(\eta)}{d\eta}
\end{aligned}
\tag{A.12}
$$

$$
\begin{aligned}
n_{2,mm}(\eta) = {} & -\frac{1}{J^{n_e}(\eta)}\frac{dx_{1,mm}(\eta)}{d\eta} + \frac{1}{(J^{n_e}(\eta))^2}\Bigg[2J^{n_e}_{,m}(\eta)\frac{dx_{1,m}(\eta)}{d\eta} \\
& + J^{n_e}_{,mm}(\eta)\frac{dx_1(\eta)}{d\eta}\Bigg] - 2\frac{(J^{n_e}_{,m}(\eta))^2}{(J^{n_e}(\eta))^3}\frac{dx_1(\eta)}{d\eta}
\end{aligned}
\tag{A.13}
$$

References

[1] C. Su, S. Zhao, and H. Ma. Reliability analysis of plane elasticity problems by stochastic spline fictitious boundary element method. *Engineering Analysis with Boundary Elements*, 36(2):118–124, 2012. ISSN 09557997. doi: 10.1016/j.enganabound.2011.07.015.

[2] X. Du. Probabilistic engineering design, 2005. URL `http://web.mst.edu/~dux/repository/me360/me360_presentation.html`.

[3] A. Haldar and S. Mahadevan. *Probability, Reliability and Statistical Methods in Engineering Design.* John Wiley and Sons, 1999.

[4] R. Melchers. *Structural Reliability Analysis and Prediction.* John Wiley and Sons, 1999.

[5] X. Huang and M. H. Aliabadi. A boundary element method for structural reliability. *Key Engineering Materials*, 627:453–456, 2015.

[6] L. Morse, Z. Sharif Khodaei, and M. H. Aliabadi. Multi-fidelity modeling-based structural reliability analysis with the boundary element method. *Journal of Multiscale Modelling*, 8(3), 2017. ISSN 1756-97371756-9745. doi: 10.1142/s1756973717400017.

[7] E. D. Leonel and W. S. Venturini. *Probabilistic fatigue crack growth using BEM and reliability algorithms*, volume 1, pages 3–14. 2011. ISBN 1743-355X 1746-4064. doi: 10.2495/be110011.

[8] X. Huang and M. H. Aliabadi. Probabilistic fracture mechanics by the boundary element method. *International Journal of Fracture*, 171(1):51–64, 2011. ISSN 0376-9429 1573-2673. doi: 10.1007/s10704-011-9625-7.

[9] E. D. Leonel, A. Chateauneuf, and W. S. Venturini. Probabilistic crack growth analyses using a boundary element model: Applications in linear elastic fracture and fatigue problems. *Engineering Analysis with Boundary Elements*, 36(6):944–959, 2012. ISSN 09557997. doi: 10.1016/j.enganabound.2011.12.016.

[10] H. L. Oliveira, A. Chateauneuf, and E. D. Leonel. Probabilistic mechanical modelling of concrete creep based on the boundary element method. *Advances in Structural Engineering*, 22(2):337–348, 2018. ISSN 1369-4332 2048-4011. doi: 10.1177/1369433218788088.

[11] C. Su and J. Xu. Reliability analysis of reissner plate bending problems by stochastic spline fictitious boundary element method. *Engineering Analysis with Boundary Elements*, 51:37–43, 2015. ISSN 09557997. doi: 10.1016/j.enganabound.2014.10.006.

[12] H. L. Oliveira, A. Chateauneuf, and E. D. Leonel. Boundary element method applied to decision-making problems involving geometric variabilities in topology optimization. *Engineering Analysis with Boundary Elements*, 85:116–126, 2017. ISSN 09557997. doi: 10.1016/j.enganabound.2017.09.016.

[13] X. Huang. *Proabilistic fracture mechanics by boundary element method.* Thesis, 2010.

[14] D. Won Kim and B. Man Kwak. Reliability-based shape optimization of two-dimensional elastic problems using bem. *Computers and Structures*, 60(5):743–750, 1995.

[15] J. Iott, R. T. Haftka, and H. M. Adelman. Selecting step sizes in sensitivity analysis by finite difference. Report, National Aeronautics and Space Administration, 1985.

[16] M. H. Aliabadi. *The Boundary Element Method: Applications in solids and structures*, volume 2. John Wiley and Sons, 2002.

[17] L. Yu, Purnendu K. Das, and Y. Zheng. A response surface approach to fatigue reliability of ship structures. *Ships and Offshore Structures*, 4(3):253–259, 2009. ISSN 1744-5302 1754-212X. doi: 10.1080/17445300902872010.

[18] B. Gaspar, C. Bucher, and C. Guedes Soares. Reliability analysis of plate elements under uniaxial compression using an adaptive response surface approach. *Ships and Offshore Structures*, 10(2):145–161, 2014.

[19] S. Hassanien, M. Kainat, S. Adeeb, and D. Langer. On the use of surrogate models in reliability-based analysis of dented pipes. In *11th International Pipeline Conference*, 2016.

[20] J. P. Lefebvre, B. Dompierre, A. Robert, M. Le Bihan, E. Wyart, and C. Sainvitu. Failure probability assessment using co-kriging surrogate models. *Procedia Engineering*, 133:622–630, 2015. ISSN 18777058. doi: 10.1016/j.proeng.2015.12.640.

[21] G. Su, L. Peng, and L. Hu. A gaussian process-based dynamic surrogate model for complex engineering structural reliability analysis. *Structural Safety*, 68:97–109, 2017.

[22] Z. Sun, J. Wang, R. Li, and C. Tong. Lif: A new kriging based learning function and its application to structural reliability analysis. *Reliability Engineering and System Safety*, 157:152–165, 2017.

[23] M. Papadrakakis, V. Papadopoulos, and N. D. Lagaros. Structural reliability analysis of elastic-plastic structures using neural networks and monte carlo simulation. *Computer Methods in Applied Mechanics and Engineering*, 136(1-2):145–163, 1996.

[24] M. Papadrakakis and N. D. Lagaros. Reliability-based structural optimization using neural networks and monte carlo simulation. *Computer Methods in Applied Mechanics and Engineering*, 191(32):3491–3507, 2002.

[25] T. Simpson, V. Toropov, V. Balabanov, and F. Viana. Design and analysis of computer experiments in multidisciplinary design optimization: A review of how far we have come - or not. 2008. doi: 10.2514/6.2008-5802.

[26] A. Bhosekar and M. Ierapetritou. Advances in surrogate based modeling, feasibility analysis, and optimization: A review. *Computers and Chemical Engineering*, 108:250–267, 2018. ISSN 00981354. doi: 10.1016/j.compchemeng.2017.09.017.

[27] R. Vitali, R. T. Haftka, and B. V. Sankar. Multi-fidelity design of stiffened composite panel with a crack. *Structural and Multidisciplinary Optimization*, 23(5):347–356, 2002. ISSN 1615-147X 1615-1488. doi: 10.1007/s00158-002-0195-1.

[28] G. Sun, G. Li, S. Zhou, W. Xu, X. Yang, and Q. Li. Multi-fidelity optimization for sheet metal forming process. *Structural and Multidisciplinary Optimization*, 44(1):111–124, 2010. ISSN 1615-147X 1615-1488. doi: 10.1007/s00158-010-0596-5.

[29] A. J. Keane, A. Sbester, and A. I. J. Forrester. Multi-fidelity optimization via surrogate modelling. *Proceedings of the Royal Society A: Mathematical, Physical and Engineering Sciences*, 463(2088):3251–3269, 2007. ISSN 1364-5021 1471-2946. doi: 10.1098/rspa.2007.1900.

[30] P. Perdikaris, D. Venturi, J. O. Royset, and G. E. Karniadakis. Multi-fidelity modelling via recursive co-kriging and gaussian-markov random fields. *Proc Math Phys Eng Sci*, 471(2179):20150018, 2015.

[31] R. Rackwitz and B. Fiessler. Structural reliability under combined random load sequences. *Computers and Structures*, 9(5):484–494, 1978.

[32] K. Breitung. Asymptotic approximations for multinormal integrals. *Journal of Engineering Mechanics*, 110(3):357–366, 1984.

[33] R. Rackwitz. Reliability analysis - a review and some perspectives. *Structural Safety*, 23(4):365–395, 2001.

[34] F. Viana. Things you wanted to know about the latin hypercube design and were afraid to ask. In *10th World Congress on Structural and Multidisciplinary Optimization*.

[35] T. Simpson. Comparison of response surface and kriging models in the mutlidisiplinary design or and aerospike nozzle. Report, Institue for Computer Applications in Science and Engineering, 1998.

[36] S. N. Lophaven, H. B. Nielsen, and J. Sondergaard. Dace: A matlab kriging toolbox, 2011. URL `http://www2.imm.dtu.dk/projects/dace/`.

[37] J. D. Martin and T. W. Simpson. Use of kriging models to approximate deterministic computer models. *AIAA Journal*, 43(4):853–863, 2005. ISSN 0001-1452 1533-385X. doi: 10.2514/1.8650.

[38] P. P. Benham, R. J. Crawford, and C. G. Armstrong. *Mechanics of Engineering Materials*. Prentice Hall, 1996.